The Astrophysical Journal, 928:53 (21pp), 2022 March 20 https://doi.org/10.3847/1538-4357/ac38a6

Nonaxisymmetric Precession of Magnetars and Fast Radio Bursts

I. Wasserman[1,2], J. M. Cordes[1], S. Chatterjee[1], and G. Batra[1]
[1] Cornell Center for Astrophysics and Planetary Science, Cornell University, NY, USA; ira@astro.cornell.edu
[2] Laboratory for Elementary Particle Physics, Cornell University, NY, USA
Received 2021 August 3; revised 2021 October 21; accepted 2021 November 9; published 2022 March 25

Abstract

The repeating fast radio bursts (FRBs) 180916.J0158 and 121102 are visible during periodically occurring windows in time. We consider the constraints on internal magnetic fields and geometries if the cyclical behavior observed for FRB 180916.J0158 and FRB 121102 is due to the precession of magnetars. In order to frustrate vortex line pinning we argue that internal magnetic fields must be stronger than about 10^{16} G, which is large enough to prevent superconductivity in the core and destroy the crustal lattice structure. We conjecture that the magnetic field inside precessing magnetars has three components: (1) a dipole component with characteristic strength $\sim 10^{14}$ G; (2) a toroidal component with characteristic strength $\sim 10^{15}$–10^{16} G that only occupies a modest fraction of the stellar volume; and (3) a disordered field with characteristic strength $\sim 10^{16}$ G. The disordered field is primarily responsible for permitting precession, which stops once this field component decays away, which we conjecture happens after ∼1000 yr. Conceivably, as the disordered component damps bursting activity diminishes and eventually ceases. We model the quadrupolar magnetic distortion of the star, which is due to its ordered components primarily, as triaxial and very likely prolate. We address the question of whether the spin frequency ought to be detectable for precessing, bursting magnetars by constructing a specific model in which bursts happen randomly in time with random directions distributed in or between cones relative to a single symmetry axis. Within the context of these specific models, we find that there are precession geometries for which detecting the spin frequency is very unlikely.

Unified Astronomy Thesaurus concepts: High energy astrophysics (739); Transient sources (1851)

1. Introduction

The relatively long 16.4 day period of FRB 180916.J0158 (CHIME/FRB Collaboration et al. 2020) and the even longer 160 day period of FRB 121102 (e.g., Cruces et al. 2021) suggest the precession of magnetars deformed by strong internal magnetic fields (Levin et al. 2020; Zanazzi & Lai 2020). However, to date no evidence for a spin period has been reported for either of these fast radio bursts (FRBs) (e.g., Zhang et al. 2018; Li et al. 2021). One possibility is that not enough bursts have been detected yet for either FRB to reveal its spin frequencies, presuming that the underlying engine is a magnetar. But a second possibility is that the physical nature of repeating bursts might prevent detecting a spin frequency even in upcoming surveys that will detect far larger numbers of individual outbursts.

The important phenomenological questions motivating this paper are as follows:

1. Should the spin period be detectable in FRBs that reappear periodically because of precession?
2. Is it possible for there to be no evidence for either a spin period or a precession period for FRBs associated with a precessing magnetar?

Recently, evidence for a short ≈0.2 s period has been presented by The CHIME/FRB Collaboration et al. (2021) from analysis of the light curve of a *single* outburst lasting ≈4 s. This report lends urgency to addressing these two questions, and raises other issues we shall not address here, such as whether the 0.2 s period is due to magnetar spin, and, if it is, what the implications are for spindown, internal magnetic fields, and precession.

In order to address these two questions, we first examine what the detection of precession tells us about the internal magnetic fields of magnetars presumed to be sources of FRBs. Shaham (1977) showed that the pinning of (crustal) superfluid neutron vortex lines can prevent slow precession, and Link (2003) showed that the pinning of neutron vortices to flux tubes associated with a proton superconductor is likely wherever the superfluid and the superconductor coexist in the core of a neutron star. Moreover, for a neutron star rotating with period P and precessing with period P_p the moment of inertia of the region where neutron vortices are pinned must be $\lesssim P/P_p \approx 10^{-7}P(\mathrm{s})/(P_p/100\,\mathrm{days})$ times the total moment of inertia of the star for slow precession to be possible. We cannot rule out that FRB 121102 and FRB 180916.J0158 are both fine-tuned to the accuracy necessary to permit slow precession. However, we regard it as far likelier that the magnetic fields in the interiors of these magnetars are large enough to destroy proton superconductivity (and perhaps even neutron superfluidity).

Section 2.1 is devoted to discussing constraints on internal magnetic fields that would be consistent with precession. We propose a specific model for the magnetic field that has three distinct components: in order of typical magnetic field strength these are a dipole field, a toroidal field (both of which are ordered), and a disordered field. We develop this model in Section 2.2, where we are led inevitably to the conclusion that the quadrupole distortion of the star is triaxial, and most likely somewhat prolate. We also propose that a magnetar may only precess for a relatively short portion of its life lasting perhaps 1000 yr.

Section 2.3 develops results on triaxial precession necessary for the more phenomenological modeling done in Section 3. In particular, we show that rather large amplitude precession can be excited with relatively little fractional expenditure of magnetic energy, a natural consequence of the fact that magnetic energy is substantially larger than rotational energy in magnetars. We also consider two distinct types of effects due to spindown. In Section 2.4 we develop the timing model relating observer time to precession phase when spindown is included. There are two effects, the familiar long-term spindown and a cyclical effect specific to precessing pulsars that has period P_p (Cordes 1993). In Section 2.5 we investigate the secular effect of spindown on the precession amplitude and phase, generalizing work done by Goldreich (1970) for oblate axisymmetric precession to triaxial precession. We outline a simple phase diagram for this more complicated problem, which is more complex than what arises for oblate, axisymmetric precession.

Finally, in Section 3 we develop a very specific model in which we assume that FRBs are tied to magnetar outbursts that occur randomly in time and point in random directions about some reference axis, which we take to be (but need not be) the magnetic dipole axis. We show that it is impossible to detect either the spin frequency or the precession period if the outbursts can point in any direction, which is not a big surprise. However, we also find that the spin frequency ought to be easy to detect in some cases and much harder to detect in others, depending on specific characteristics of the precession model and the distribution of beam directions of the outbursts.

From a qualitative point of view, we offer two simple reasons why the outbursts underlying FRBs may occur randomly in time. Although tautological, one explanation is that the physical mechanism triggering the bursts simply is stochastic temporally, with burst directions that are random within some boundaries. Another is that the times between burst triggers are irregular but correlated, perhaps because there is a characteristic time for the burst phenomenon to reload, but associated with each outburst is a random time offset, possibly as large as the spin period, related to where the burst is triggered within the magnetar magnetosphere. The bursts may point in a large range of directions because they involve plasma moving relativistically along open magnetic field lines, leading to highly focused energy output in directions ranging from close to the magnetic dipole axis to perpendicular to the light cylinder. Alternatively, bursts may originate from a set of distinct, concentrated regions in the magnetosphere of a magnetar that turn on and off stochastically, with each region beaming energy outward in a different direction.

In a companion paper (Cordes et al. 2021) we address the challenge of uncovering an underlying FRB spin frequency in a more general, phenomenological way that does not rely on as specific a model for bursts from rotating magnetars as we develop in Section 3. The model presented in this paper can be regarded as a definite physical setup that realizes the general conditions for hiding the spin frequency of an FRB-inducing magnetar developed in the companion paper.

2. Internal Magnetic Fields and Triaxial Precession

2.1. Internal Magnetic Fields that Permit Slow Precession

Previous work has focused primarily on precession arising from oblate axisymmetric distortion due to magnetic stresses (e.g., Levin et al. 2020; Zanazzi & Lai 2020). Here, we examine what internal magnetic structure may be required for precession to occur, and highlight distinctive features that arise when the distortion is not axisymmetric and possibly prolate.

The internal magnetic structure of magnetars is not well studied. In general, magnetohydrodynamic (MHD) studies of magnetic fields in normal conductors have shown that there are *no* stable magnetic field configurations in barotropic normal fluids (Lander & Jones 2012; Mitchell et al. 2015), but that stable, axisymmetric configurations may exist in stably stratified fluids (Reisenegger 2009; Akgün et al. 2013; Mitchell et al. 2015). Braithwaite (2009) and Akgün et al. (2013) argued that there may be stable magnetic field configurations in stably stratified stars whose poloidal fields are *much weaker* than their toroidal fields. Glampedakis & Lasky (2016) argued that the *equilibrium* magnetic fields in nonbarotropic normal-fluid stars can be specified freely if they are axisymmetric, but not if they are nonaxisymmetric. At the strong fields we envision, magnetization due to Landau quantization of core electrons also affects stability (Suh & Mathews 2010; Rau & Wasserman 2021). Relativistic equilibria have been computed using realistic equations of state (e.g., Cardall et al. 2001; Kiuchi & Yoshida 2008; Frieben & Rezzolla 2012); equilibria were only found to exist if the maximum internal magnetic field strength is $\lesssim 10^{18}$ G, which is a significant indication of limitations imposed by the overall dynamical stability, but does not assess MHD stability. Of course, stability constraints are not necessarily relevant if the magnetic field is time-dependent, although presumably field configurations that are MHD-unstable vary rather rapidly on timescales set by the local Alfvèn speed and the length scale of variation.

Overall, these studies suggest that the internal magnetic fields of magnetars could be considerably stronger than their dipole (surface) magnetic fields.

Another, rather different argument also suggests strong internal magnetic fields. Once the core of the star cools below $\approx 10^9$ K core protons become superconducting unless the internal magnetic field is stronger than the second critical field strength:

$$H_{c2} = \frac{\Phi_0}{2\pi\xi_p^2} = \frac{(\pi m_p^\star \Delta_p / p_{\mathrm{F},p})^2 c}{2e\hbar} \approx \frac{9\times 10^{15}(\Delta_p/m_e)^2 (m_p^\star/0.7m_p)^2}{(p_{\mathrm{F},p}/\ 100\ \mathrm{MeV})^2}\ \mathrm{G} \quad (1)$$

where Δ_p is the proton gap, $p_{\mathrm{F},p}$ is the proton Fermi momentum, $m_p^\star$ is the proton effective mass, $\xi_p = \hbar p_{\mathrm{F},p}/\pi m_p^\star \Delta_p$ is the coherence length, and $\Phi_0 = \pi\hbar c/e$ is the flux quantum. Proton gap calculations are complicated by many-body effects at high densities (Zuo et al. 2008; Gezerlis et al. 2014; Dong et al. 2017; Guo et al. 2019) but indicate that $\Delta_p \simeq 0.5\ \mathrm{MeV} \approx m_e$ near nuclear density $n_{\mathrm{nuc}} = 0.16\ \mathrm{fm}^{-3}$, where $p_{\mathrm{F},p} \approx 100\ \mathrm{MeV}$; Δ_p decreases to zero at densities $\gtrsim 2n_{\mathrm{nuc}}$. Of course, it is also possible that protons are superconducting but magnetic field strengths at the inner boundary of the (normal) crust are below the first critical field strength:

$$H_{c1} \approx \frac{2\times 10^{14}(p_{\mathrm{F},p}/100\ \mathrm{MeV})^3 \ln\kappa}{(m_p^\star/0.7m_p)}\ \mathrm{G},$$

$$\kappa \approx \frac{4.8(m_p^\star/0.7m_p)^{3/2}(\Delta_p/m_e)}{(p_{\mathrm{F},p}/100\ \mathrm{MeV})^{5/2}},$$

in which case magnetic fields would not penetrate into the superconductor in equilibrium if entering from the outside. However, it is very likely that the magnetic flux in the core is "left over" from before it cooled enough to become superconducting (e.g., Baym et al. 1969), in which case the proton superconductor in the core is in a "mixed state" with $H_{c2} > H > H_{c1}$. Quadrupolar deformations due to magnetic fields are

$$\epsilon_{\rm mag} = \frac{\beta_2 HBR^4}{GM^2} \approx \frac{2 \times 10^{-6}\beta_2 B_{15}^2 R_{10}^4}{M_{1.4}^2} \times \frac{H}{B} \qquad (2)$$

for magnetic induction $B = 10^{15}B_{15}$ G, stellar radius $R = 10R_{10}$ km, and mass $M = 1.4M_{1.4}\ M_\odot$, where $H/B = 1$ for a normal conductor but $H/B > 1$ for a type II superconductor (e.g., Jones 1975; Cutler 2002; Wasserman 2003; Akgün & Wasserman 2008; Henriksson & Wasserman 2013). The parameter β_2 depends on the structure of the neutron star and of its internal magnetic field, and represents how effectively the magnetic forces cause quadrupolar deformation.

The superconductor is type II as long as $\kappa > 1/\sqrt{2}$, which is the case throughout much of the region where protons are superconducting. In a type II superconductor, magnetic flux is organized into an array of thin flux tubes that have an areal density $eB/\pi\hbar c \approx 5 \times 10^{21}B_{15}\,{\rm cm}^{-2}$. If the neutrons are also superfluid their vorticity would be confined into thin vortex lines with a much lower areal density $\mu_n\Omega/\pi\hbar \approx 3 \times 10^4(\mu_n/m_n)/P({\rm s})\,{\rm cm}^{-2}$ for a rotation period P(s), where μ_n/m_n is the neutron chemical potential in units of the neutron rest mass. Unless the relative velocity between flux lines and vortex lines is high enough, which may be true if the precession amplitude remains sufficiently large (Link & Cutler 2002), vortex lines will pin to flux lines (Link 2003), which frustrates slow precession (Shaham 1977). This problem can be avoided entirely if the core of the neutron star is hot enough that neutrons remain normal: neutron gaps are $\sim$10–100 keV $\simeq 10^{8-9}$ K (Zuo et al. 2008; Gezerlis et al. 2014; Dong et al. 2017; Guo et al. 2019). Calculations by Potekhin & Chabrier (2018) indicate that the core of a magnetar may cool below a few 10^8 K within $\lesssim$100 yr of forming, so neutrons may be normal in some but not all of the core of a $\lesssim$100 yr old magnetar unless the maximum neutron critical temperature in the core is lower than current estimates. But even a moderately small region where protons and neutrons are both superfluid could have an important impact on neutron star precession: for a precession period P_p the moment of inertia I_p of any region in the core where vortices are pinned to proton flux tubes must be $\lesssim P/P_p \simeq 10^{-5}P({\rm s})/P_p({\rm days})$ times the total moment of inertia of the star (Shaham 1977).

Here, we assume that the magnetic field in the core is strong enough to suppress superconductivity entirely. This means that we suppose that the total magnetic field strength $B = H > H_{c2}$ throughout all of the core. For this to be true, the internal field strength must be at least comparable to and probably larger than the dipole magnetic field at the stellar surface. This may be achieved if there are substantial nondipolar components of the internal magnetic field, particularly toroidal components (e.g., Cutler 2002). Akgün et al. (2013) found stable, axisymmetric equilibria with toroidal fields $\lesssim 100$ times stronger than the poloidal fields. The deformation due to toroidal fields can be axisymmetric, but if so, it is *prolate* rather than *oblate*.

Vortex line pinning may also be a problem in the neutron star crust, where neutron pairing is S-wave and superfluid gaps are larger, $\sim$MeV (Gezerlis et al. 2014); neutrons are likely to be superfluid down to densities close to neutron drip for temperatures $\sim$ a few 10^8 K (Potekhin & Chabrier 2018). The unpinning and repinning of neutron superfluid vortices to crustal nuclei have long been thought to be responsible for the behavior of pulsar spins during and after rotational glitches (Anderson & Itoh 1975; Anderson et al. 1982; Alpar et al. 1984; Link et al. 1993). Strong magnetic fields alter the equation of state because the degenerate electron gas becomes one-dimensional once

$$\frac{p_{\rm F}}{m_e c} \lesssim \sqrt{\frac{2eB\hbar}{m_e^2 c^3}} = 6.7\sqrt{B_{15}}\ ;$$

the equation of state of the inner crust is largely unaffected for $B \lesssim 10^{17}$ G, although it stiffens considerably in the outer crust (Mutafchieva et al. 2019). The crust ought to crystallize except at low densities for temperatures $\lesssim$ a few 10^9 K (Carreau et al. 2020). Neutron star precession can only persist in spite of the potential pinning of neutron superfluid vortex lines to crustal nuclei or pasta phases (Ravenhall et al. 1983; Hashimoto et al. 1984; Lorenz et al. 1993) if the sustained precession amplitude is large enough (Link & Cutler 2002). The complex topology of the nuclear pasta revealed by molecular dynamics simulations (Schneider et al. 2018) could complicate pinning.

There are two other effects of superstrong crustal magnetic fields that should alter the physical conditions there, perhaps enabling precession to occur. One effect is to shatter the crystalline crust, which can happen if $B^2/8\pi > \mu_{\rm el}$, where $\mu_{\rm el}$ is the elastic shear modulus. Molecular dynamics simulations by Caplan et al. (2018) indicate that the shear modulus of nuclear pasta is $\lesssim 10^{31}{\rm erg\,cm}^{-3} \equiv (1.6 \times 10^{16}{\rm G})^2/8\pi$, so crustal magnetic fields $\gtrsim 10^{16}$ G would shatter the crust (see also Pethick & Potekhin 1998).

A second possibility presents itself for magnetic fields larger than the Clogston–Chandrasekhar limiting field strength (Clogston 1962; Chandrasekhar 1962)

$$B_{\rm CC} = \frac{\Delta_n}{\mu_n\sqrt{2}} \approx 1.2 \times 10^{17}\Delta_n({\rm MeV})\ {\rm G} \qquad (3)$$

above which flipping the spin of one neutron can break an S-wave Cooper pair; here Δ_n is the neutron gap and μ_n is the neutron magnetic moment. For such large magnetic field strengths, the uniform S-wave BCS superfluid condensate transitions to an inhomogeneous LOFF state (Larkin & Ovchinnikov 1974; Fulde & Ferrell 1964; Kinnunen et al. 2018). Although the implications of such states in the crust have not been explored extensively, it is conceivable that the inhomogeneous LOFF state behaves more like a crystal than like a (super)fluid, which may permit precession to occur (Lee et al. 2018). Moreover, somewhat weaker magnetic fields may destroy the predominantly P-wave superfluidity of core neutrons for which $\Delta_n \lesssim 100$ keV (e.g., Haskell & Sedrakian 2018).

In any event, we conclude that magnetic fields stronger than about 10^{16} G are necessary for slow precession. However, the precession period is of the order of

$$P_p \sim \frac{P}{\epsilon_{\rm mag}} \sim \frac{100\ {\rm days}\ P({\rm s})}{10^7\epsilon_{\rm mag}} \qquad (4)$$

which, in view of Equation (2), suggests a quadrupolar deformation corresponding to $B \sim 10^{14}$–10^{15} G for FRB 121102 and FRB 180916.J0158+65, which is too weak to prevent the superconductivity of core protons according to Equation (1). We therefore propose that the magnetic fields inside these magnetars consist of three components:

1. a dipole field with characteristic strength $B_D \sim 10^{14}$ G;
2. a quadrupolar field with characteristic strength $B_T \sim (10^{15}$–$10^{16})$ G and a symmetry axis misaligned with the dipole moment; and
3. a disordered magnetic field with characteristic strength $B_{\rm turb} \sim 10^{16}$ G strong enough to suppress superconductivity but with large-scale stresses that do not contribute significantly to the quadrupolar deformation of the star.

The spindown timescale in this model is of the order of

$$t_{\rm sd} = \frac{I_0 c^3 P^2}{4\pi^2 B_D^2 R^6} \approx \frac{2 \times 10^3 \text{ yr } I_{0,45}[P(\text{s})]^2}{B_{D,14}^2 R_{10}^6} \tag{5}$$

where $I_0 = 10^{45} I_{0,45}$ g cm^2 is the moment of inertia of the star and $B_D = 10^{14} B_{D,14}$ G; the expected ratio of the spindown timescale to the precession period is

$$\frac{t_{\rm sd}}{P_p} = \left(\frac{c^3 P}{4\pi^2 GM}\right)\left(\frac{B}{B_D}\right)^2\left(\frac{I_0}{MR^2}\right) \simeq \frac{7 \times 10^4 P(\text{s})}{M_{1.4}}\left(\frac{B}{10 B_D}\right)^2\left(\frac{I_0}{0.2 MR^2}\right) \tag{6}$$

so spindown is very slow compared with precession. Below, we shall also suggest that $B_{\rm turb}$ decays via ambipolar diffusion within ∼100–1000 yr. That would mean that if FRB 121102 and FRB 180916.J0158+65 have $P \simeq 10$ s they are both younger than their spindown ages and spinning close to their original rotational frequencies. However if they are spinning faster, with $P \simeq 1$ s then they might be about as old as their spindown ages, have quadrupolar distortions $\epsilon_{\rm mag} \sim 10^{-7}$, and be of order halfway through their lifetimes as precessing neutron stars.

2.2. Magnetic Precession

In this paper, we consider triaxial magnetic distortions that may be far from oblate. We shall see that such configurations lead to qualitatively new features for neutron star precession that may have distinctive observable consequences. Precession of a fluid star caused by magnetic distortions differs qualitatively from solid-body precession even though mathematically the two are the same. The inevitability of precession for stars with nonaligned spin and magnetic fields was originally pointed out by Spitzer (1958), and was studied extensively by Mestel and collaborators (Mestel & Takhar 1972; Mestel et al. 1981; Nittmann & Wood 1981). These studies also found that there are slow, internal nonrigid motions in addition to uniform rotation, which have been studied recently by Lander & Jones (2017) for neutron stars with toroidal magnetic fields. Below, we neglect these motions, which are second-order in small quantities, although we recognize that they may be significant for magnetic field evolution.

In a rotating, highly magnetic fluid the matter density is perturbed away from spherical symmetry. The moment of inertia tensor of the star only depends on the $l = 2$ perturbations:

$$I_{ij} = I_0\left[\delta_{ij} + \epsilon_{\rm rot}\left(\frac{1}{3}\delta_{ij} - \hat{\mathbf{\Omega}}_i\hat{\mathbf{\Omega}}_j\right) + \epsilon_{\rm mag} m_{ij}\right] \tag{7}$$

where rotation is along the $\hat{\mathbf{\Omega}}$ direction, $\epsilon_{\rm rot}$ and $\epsilon_{\rm mag}$ are the amplitudes of the $l = 2$ distortions due to rotation and magnetic fields, respectively, and m_{ij} is symmetric and trace-free (STF). The stellar angular momentum is

$$L_i = I_{ij}\Omega_j = I_0\left[\left(1 - \frac{2\epsilon_{\rm rot}}{3}\right)\Omega_i + \epsilon_{\rm mag} m_{ij}\Omega_j\right] \equiv I_0'(\delta_{ij} + \epsilon'_{\rm mag} m_{ij})\Omega_j, \tag{8}$$

where we use the summation convention. Since $\epsilon'_{\rm mag} = \epsilon_{\rm mag}[1 + \mathcal{O}(\epsilon_{\rm rot})]$ we ignore the difference between $\epsilon_{\rm mag}$ and $\epsilon'_{\rm mag}$ below. Invert Equation (8) to get $\Omega_j = L_i(\delta_{ij} - \epsilon_{\rm mag} m_{ij})/I_0'$ to first order in small quantities. Since $\epsilon_{\rm mag} m_{ij}$ is STF

$$\epsilon_{\rm mag} m_{ij} = -\frac{\epsilon}{2}(\delta_{ij} - \hat{\boldsymbol{e}}_{3,i}\hat{\boldsymbol{e}}_{3,j}) + \epsilon\hat{\boldsymbol{e}}_{3,i}\hat{\boldsymbol{e}}_{3,j} + \Delta\epsilon(\hat{\boldsymbol{e}}_{1,i}\hat{\boldsymbol{e}}_{1,j} - \hat{\boldsymbol{e}}_{2,i}\hat{\boldsymbol{e}}_{2,i}); \tag{9}$$

for an axisymmetric magnetic field $\Delta\epsilon = 0$ but we regard this case as exceptional (although Spitzer (1958) and Mestel & Takhar (1972) and subsequent work focused on this situation). Since $\hat{\boldsymbol{e}}_3$ is fixed in the rotating frame of reference

$$\frac{d\hat{\boldsymbol{e}}_3}{dt} = \left(1 - \frac{\epsilon}{2}\right)\frac{\boldsymbol{L} \times \hat{\boldsymbol{e}}_3}{I_0'} - \frac{\Delta\epsilon(L_1\hat{\boldsymbol{e}}_2 + L_2\hat{\boldsymbol{e}}_1)}{I_0'} \Rightarrow \frac{d(\hat{\boldsymbol{e}}_3 \cdot \boldsymbol{L})}{dt} = -\frac{2\Delta\epsilon L_1 L_2}{I_0'} \tag{10}$$

in the inertial frame. If the star is axisymmetric, precession is about the magnetic field axis of symmetry, as is well known (e.g., Spitzer 1958; Goldreich 1970; Mestel & Takhar 1972), but this is untrue for the more general nonaxisymmetric case, where precession is more complicated.

For the intense magnetic fields we envision, the main cause of quadrupolar deformations is magnetic stresses. Even in nonbarotropic stars, the magnetic field configurations that give rise to *static* deformations are highly constrained (Glampedakis & Lasky 2016). In such a star, the static structure is perturbed away from spherical symmetry by the Lorentz force density $\boldsymbol{f}_{\rm L}$; to linear order

$$0 = -\boldsymbol{\nabla}\delta P + \hat{\boldsymbol{r}} g_0(r)\delta\rho - \rho_0(r)\boldsymbol{\nabla}\delta\Psi + \boldsymbol{f}_{\rm L} + \boldsymbol{f}_{\rm NF} \tag{11}$$

where $g_0(r) = -GM(r)/r^2$ is the gravitational acceleration in the unperturbed star, $\delta P(\boldsymbol{r})$ is the pressure perturbation, $\boldsymbol{f}_{\rm NF}$ is due to nonfluid forces, and $\delta\Psi$ is the gravitational potential of the perturbation. In the neutron star core, where $\boldsymbol{f}_{\rm NF} = 0$, axisymmetric static perturbations require that the toroidal field be

$$\boldsymbol{B}_T = B_T(r, \theta)\hat{\boldsymbol{\varphi}} = \frac{f(\psi)\hat{\boldsymbol{\varphi}}}{r\sin\theta}$$

where $\psi(r, \theta)$ is the flux function of the poloidal field

$$\boldsymbol{B}_P = \frac{\boldsymbol{\nabla}\psi \times \hat{\boldsymbol{\varphi}}}{r \sin\theta},$$

but for nonaxisymmetric fields $f'(\psi) =$ constant (Glampedakis & Lasky 2016). Assuming that this restriction holds, Equation (11) is easy to solve in a nonbarotropic star, where δP and $\delta\rho$ are unrelated.

Lasky & Melatos (2013) considered a specific example of a nonaxisymmetric field with dipole and toroidal fields that have different axes of symmetry $\hat{\boldsymbol{\mu}}$ and $\hat{\boldsymbol{t}}$, respectively, that lead to static deformations of the star. Below, we use a slightly different model for the dipole and toroidal fields, and also include a disordered component. Assuming that the quadrupolar deformation due to the disordered component is relatively small, magnetic forces due to the ordered dipole and toroidal fields result in a perturbed moment of inertia tensor

$$\delta I_{ij} = q_T\left(\frac{\delta_{ij}}{3} - \hat{\boldsymbol{t}}_i\hat{\boldsymbol{t}}_j\right) + q_D\left(\hat{\boldsymbol{\mu}}_i\hat{\boldsymbol{\mu}}_j - \frac{\delta_{ij}}{3}\right). \tag{12}$$

Both q_T and q_D are positive, and it follows that the toroidal field promotes prolate deformations relative to a symmetry axis $\hat{\boldsymbol{t}}$ whereas the dipole field promotes oblate deformations relative to a symmetry axis $\hat{\boldsymbol{\mu}}$. If we assume that

$$\hat{\boldsymbol{\mu}} = \cos\sigma\hat{\boldsymbol{t}} + \sin\sigma\hat{\boldsymbol{u}} \tag{13}$$

in a right-handed $\hat{\boldsymbol{u}}$, $\hat{\boldsymbol{v}}$, $\hat{\boldsymbol{t}}$ coordinate system then we find that the eigenvalues of δI_{ij} are

$$\lambda_\pm = q_T\left[-\frac{1-d}{6} \pm \sqrt{\left(\frac{1-d}{2}\right)^2 + d\sin^2\sigma}\,\right]$$
$$\lambda_v = \frac{q_T(1-d)}{3} \tag{14}$$

where we define $q_D = dq_T$. The eigenvectors are $\hat{\boldsymbol{v}}$ for λ_v,

$$\hat{\boldsymbol{e}}_+ = \frac{\hat{\boldsymbol{u}}\{(1-d)/2 + d\sin^2\sigma + \sqrt{[(1-d)/2]^2 + d\sin^2\sigma}\,\} + \hat{\boldsymbol{t}}d\sin\sigma\cos\sigma}{\sqrt{2\{[(1-d)/2]^2 + d\sin^2\sigma + [(1-d)/2 + d\sin^2\sigma]\sqrt{[(1-d)/2]^2 + d\sin^2\sigma}\,\}}} \equiv \hat{\boldsymbol{u}}\cos\zeta + \hat{\boldsymbol{t}}\sin\zeta \tag{15}$$

for λ_+, and $\hat{\boldsymbol{e}}_- = -\hat{\boldsymbol{u}}\sin\zeta + \hat{\boldsymbol{t}}\cos\zeta$ for λ_-. Because there are three different eigenvalues and eigenvectors the star is triaxial: it is only axisymmetric if (i) $d = 0$ (i.e., no internal dipole field), (ii) $d = \infty$ (no internal toroidal field), or (iii) $\sigma = 0$ (aligned dipole and toroidal field symmetry axes). In general

$$\lambda_+ - \lambda_v = \sqrt{\left(\frac{1-d}{2}\right)^2 + d\sin^2\sigma} - \frac{1-d}{2} > 0$$
$$\lambda_v - \lambda_- = \sqrt{\left(\frac{1-d}{2}\right)^2 + d\sin^2\sigma} + \frac{1-d}{2} > 0 \tag{16}$$

so $\lambda_+ > \lambda_v > \lambda_-$.

For the dipole field, we adopt a stream function

$$\psi = B_D h(r/R) r^2[1 - (\hat{\boldsymbol{\mu}}\cdot\hat{\boldsymbol{r}})^2] \tag{17}$$

where $\hat{\boldsymbol{\mu}}$ is the dipole axis, and the dimensionless function is

$$h(x) = \frac{m(x)}{x^3} \tag{18}$$

for a mass profile $M(r) = Mm(r/R)$. The magnetic field matches smoothly to an exterior vacuum dipole provided that $\rho = 0$ and $d\rho/dr = 0$ at the stellar surface. Typically, the poloidal magnetic field vanishes somewhere along its equator, and is prone to instability there. In the Cowling approximation we find that

$$q_D = \frac{2\mu^2}{GM} = \frac{2B_D^2R^6}{GM} \qquad \text{[Cowling]} \tag{19}$$

independent of the detailed density profile of the star, but including self-gravity changes q_D by a factor ~ 2.

The toroidal field must vanish at the surface of the star in order to match to a vacuum exterior. The toroidal fields in a magnetar magnetosphere are much weaker than the internal toroidal fields we consider here. In corotating magnetosphere solutions, the toroidal field is $\lesssim \Omega R/c$ times weaker than the dipole field at the stellar surface (e.g., Goldreich & Julian 1969), whereas in twisted, force-free magnetosphere models the surface toroidal field may be comparable to the dipole field (Akgün et al. 2016; Mahlmann et al. 2019); for either of these magnetospheric models, the surface toroidal field is considerably weaker than it is in much of the stellar interior, where the dipole field is much weaker than the toroidal field in our picture. As a rough approximation we take the toroidal field to be zero at the surface. For $f'(\psi) =$ constant in the neutron star core, this important constraint can be satisfied in two ways that lead to very different values of q_T.

1. The toroidal field may fill the core,

$$\boldsymbol{B}_T = \frac{B_T r h(r/R)\sin\theta\hat{\boldsymbol{\varphi}}}{R} = \frac{B_T m(x)\sin\theta\hat{\boldsymbol{\varphi}}}{x^2}, \tag{20}$$

where θ is the polar angle measured from the symmetry axis of the toroidal field, $\hat{\boldsymbol{t}}$, and $\hat{\boldsymbol{\varphi}}$ encircles $\hat{\boldsymbol{t}}$. The boundary region within which the toroidal field strength drops precipitously from its value at the outer core contributes to the distortion even though it occupies a geometrically thin, low-mass shell. The value of q_T depends on the density profile; we adopt

$$\rho(r) = \rho(0)(1-x^2)^2 \;\Rightarrow\; m(x) = \frac{35x^3}{8} - \frac{21x^5}{4} + \frac{15x^7}{8} \text{ and } I_0 = \frac{2MR^2}{9} \tag{21}$$

where I_0 is the moment of inertia of the spherical star; for this particular density profile including self-gravity implies

$$q_D \simeq \frac{3.19B_D^2R^6}{GM} \;\Rightarrow\; \epsilon_{\mathrm{mag},D} \simeq \frac{14.36B_D^2R^4}{GM^2}. \tag{22}$$

To zeroth order in the shell thickness

$$q_T = \frac{0.237 B_T^2 R^6}{GM} = \frac{0.188\langle B_T^2\rangle R^6}{GM} \Rightarrow \epsilon_{\rm mag,T} = \frac{0.845\langle B_T^2\rangle^2}{GM^2} \tag{23}$$

for this model, where $\langle B_T^2\rangle = 1.26 B_T^2$ is the mean square toroidal field strength. The thin shell contributes about half of the deformation, which may be unrealistic, so actual values could be as small as half as large.

2. The toroidal field may be confined to a limited volume if instead of Equation (20)

$$\boldsymbol{B}_T = B_T\hat{\boldsymbol{\varphi}}\left[\frac{m(x)\sin\theta}{x^2} - \frac{1}{x\sin\theta}\right] \times \Theta\left(\frac{m(x)\sin\theta}{x^2} - \frac{1}{x\sin\theta}\right), \tag{24}$$

which is the model used by Lasky & Melatos (2013). (See also Akgün et al. (2013), who introduced models of this type in their study of magnetic stability in axisymmetry.) The field only occupies about 21% of the stellar volume, and has a mean square $\langle B_T^2\rangle = 0.01 B_T^2$ within this volume. In this case

$$q_T = \frac{3.53\times 10^{-4} B_T^2 R^6}{GM} = \frac{3.53\times 10^{-2}\langle B_T^2\rangle R^6}{GM} \Rightarrow \epsilon_{\rm mag,T} = \frac{1.59\times 10^{-1}\langle B_T^2\rangle R^4}{GM^2}. \tag{25}$$

The quadrupole moment for this model is diminished severely because it is confined to such a small volume.

3. Interpreting these two models as extremes for quadrupolar distortion due to toroidal fields we estimate

$$q_T \simeq \frac{(0.04 - 0.2)\langle B_T^2\rangle R^6}{GM} \tag{26}$$

and therefore

$$d = \frac{q_D}{q_T} \simeq \frac{(20-100)B_D^2}{\langle B_T^2\rangle} = \frac{(0.2-1)(10B_D)^2}{\langle B_T^2\rangle}. \tag{27}$$

Thus, $d \lesssim 1$ but is probably not well below 0.1, so the quadrupolar distortions arising from the ordered fields are significantly triaxial unless the dipole axis $\hat{\boldsymbol{\mu}}$ and toroidal axis $\hat{\boldsymbol{t}}$ are aligned perfectly, and are very likely prolate. See Equation (16).

If the toroidal field occupies a small volume, as in Equation (24), then no matter how large $\langle B_T^2\rangle$ is the field will be incapable of suppressing proton superconductivity anywhere. Even if the field occupies much of the star, as in Equation (20), it may not be strong enough to exceed H_{c2} even if it is much stronger than B_D. Moreover, as noted above $\boldsymbol{B}_P$ is prone to instability in this model. Although the toroidal field represented by Equation (24) can prevent instability in axisymmetry if $\langle B_T^2\rangle$ is large enough (Akgün et al. 2013) we doubt that the tilted dipole model is stable ($\boldsymbol{\nabla}\times\boldsymbol{B}_T \| \boldsymbol{B}_P$ for both Equations (24) and (20) in axisymmetry but not in the tilted dipole model). For these reasons we conclude that a precessing neutron star with internal fields that are stable on short timescales ought to include a disordered component with a characteristic local field strength $B_{\rm turb} > \sqrt{\langle B_T^2\rangle} > B_D$. The disordered field may be a remnant of the violent process that generated the strong internal magnetic fields (Thompson & Duncan 1993; Braithwaite 2009).

The turbulent magnetic field is

$$\boldsymbol{B}_{\rm turb} = \boldsymbol{\nabla} N_1(\boldsymbol{x}) \times \boldsymbol{\nabla} N_2(\boldsymbol{x}) \tag{28}$$

where the scalar functions $N_i(\boldsymbol{x})$ are constant along the field lines and are advected with the fluid in the limit of perfect conductivity. We can think of N_i as a pair of co-moving field line labels. We assume that the turbulence is small-scale locally but has a large-scale bias, so that we can expand

$$N_i(\boldsymbol{x}) = \frac{1}{\sqrt{V}}\sum_{\boldsymbol{k}} S_i(\epsilon\boldsymbol{x}, k)\exp[i(\boldsymbol{k}\cdot\boldsymbol{x}) + i\psi_i(\boldsymbol{k})] \tag{29}$$

where $S_i(\epsilon\boldsymbol{x}, k)$ is a spectral function and ϵ is the ratio between the small scale that characterizes the local turbulence and the large scale that characterizes the bias; V is the normalization volume and $\psi_i(\boldsymbol{k})$ is a random phase. If we assume that $\psi_1(\boldsymbol{k}) = \psi_2(\boldsymbol{k})$, which is plausible if the turbulent field results from fluid motions that stretch, twist, and fold individual field lines, then Equation (28) has a mean value $\sim\epsilon^2$ times the characteristic local field amplitude, and there are magnetic forces $\sim\epsilon$ (corresponding to the gradient of turbulent magnetic pressure), $\sim\epsilon^3$, and $\sim\epsilon^5$ (corresponding to the mean field). We assume that the local field is strong enough to destroy superconductivity, but that the forces are too weak to have much effect on quadrupolar deformation. We do not address the question of whether such a field may form and persist for $\gtrsim$years (as opposed to seconds or minutes; e.g., Thompson & Duncan 1993). However, we do hope that the stresses can act as *deus ex machina* to stabilize the ordered fields. Link & van Eysden (2016) have summarized theoretical and phenomenological arguments for the existence of a tangled field in magnetars (see also Bretz et al. 2021). Here we add another phenomenological argument that strong disordered fields pervade the core of a young magnetar: without them slow precession is not possible, necessitating some other explanation for the slow and very regular periodicities of FRB 121102 and FRB 180916.J0158+65. Moreover, before the disordered field decays away it is a substantial energy reservoir that might power FRBs.

Magnetic fields in the core of a highly magnetic neutron star containing normal neutrons and protons decay via ambipolar diffusion. Reisenegger & Goldreich (1992) estimated a decay timescale

$$t_{\rm ambip}(L) \sim \frac{220\ {\rm yr}(20Y)(T_8/3)^2[L({\rm km})]^2(n_b/n_{\rm nuc})^{2/3}}{B_{16}^2(L)}, \tag{30}$$

for fields varying on a length scale L(km), where n_b is baryon density, $n_{\rm nuc} = 0.16\,{\rm fm}^{-3}$ is nuclear density, Yn_b is proton density, and $T = 10^8 T_8$ (see also Glampedakis et al. 2011; Passamonti et al. 2017; Gusakov et al. 2017, Figure 1). Neutron superfluidity would increase the decay time but as long as the core temperature is as high as $\sim$ a few 10^8 K the normal neutron fraction will be considerable in much of the core, and Equation (30) remains true within a factor of an order of magnitude or less. (Field decay heats the core, but given the steep T dependence of neutrino cooling the core temperature is

not changed substantially.) The tangled component will decay on a timescale that depends on its fluctuation spectrum: if $B^2(L) \propto L^{\alpha}$ the decay timescale $t_{\rm ambip}(L) \propto L^{2-\alpha}$, which implies faster decay on smaller scales for $\alpha < 2$ and vice versa; theories of fully developed magnetic turbulence generally find $\alpha < 1$ (Iroshnikov 1963; Kraichnan 1965; Goldreich & Sridhar 1995). Plausibly, the tangled field decays away in time $\lesssim 10^3$ yr, after which substantial portions of the magnetar core become superconducting, which limits the time span during which a magnetar may precess slowly. The larger-scale ordered fields also decay as long as core protons are normal but since $L(\mathrm{km}) \simeq 10$ for these fields they may survive relatively undiminished until protons become superconducting, after which ambipolar diffusion becomes ineffective. Ambipolar diffusion in the crust is suppressed by neutron superfluidity. Magnetic field evolution in a magnetar crust involves an interplay among the Hall effect, ohmic dissipation, and plastic flow (Li et al. 2016; Lander & Gourgouliatos 2019), involving instabilities on timescales $\sim 10^3$ yr (Gourgouliatos & Pons 2020) and possibly evolution toward an attractor solution on timescales $\sim 10^5$ yr (Gourgouliatos & Cumming 2014a, 2014b). (The effect of the Landau quantization of crustal electrons on magnetar magnetic field evolution, which may be substantial, is being included for the first time in a forthcoming paper by P. B. Rau & Wasserman 2021, in preparation.)

2.3. Triaxial Precession

Conservation of angular momentum is

$$\frac{d\boldsymbol{L}}{dt} = \frac{d^\star \boldsymbol{L}}{dt} + \boldsymbol{\Omega} \times \boldsymbol{L} = \boldsymbol{N} \tag{31}$$

where $\boldsymbol{L}$ is the angular momentum and $\boldsymbol{N}$ is the spindown torque; $d^\star/dt$ is the time derivative in the rotating frame. Substitute $\boldsymbol{L} = L\hat{\boldsymbol{\ell}}$, where $L = |\boldsymbol{L}|$, to get

$$\frac{dL}{dt} = \frac{d^\star L}{dt} = \hat{\boldsymbol{\ell}} \cdot \boldsymbol{N} \equiv N_\parallel \,, \tag{32}$$

and

$$\frac{d^\star \hat{\boldsymbol{\ell}}}{dt} + \boldsymbol{\Omega} \times \hat{\boldsymbol{\ell}} = \frac{\boldsymbol{N} - \hat{\boldsymbol{\ell}}\hat{\boldsymbol{\ell}} \cdot \boldsymbol{N}}{L} \equiv \frac{\boldsymbol{N}_\perp}{L} \,. \tag{33}$$

For the spindown torque we adopt

$$\begin{aligned} \boldsymbol{N} &= -\frac{k\mu^2\Omega^2}{c^3}(\boldsymbol{\Omega} - a\boldsymbol{\Omega} \cdot \hat{\boldsymbol{\mu}}\hat{\boldsymbol{\mu}}) \\ \Rightarrow N_\parallel &= -\frac{k\mu^2\Omega^2}{c^3}(\hat{\boldsymbol{\ell}} \cdot \boldsymbol{\Omega} - a\boldsymbol{\Omega} \cdot \hat{\boldsymbol{\mu}}\hat{\boldsymbol{\ell}} \cdot \hat{\boldsymbol{\mu}}) \end{aligned} \tag{34}$$

where $\boldsymbol{\mu}$ is the magnetic moment of the star, and k and a are numerical constants $\sim$1; for numerical evaluations we adopt $k = 2$ and $a = 1/2$, which corresponds to a rate of energy loss $\boldsymbol{\Omega} \cdot \boldsymbol{N} = (\mu^2\Omega^4/c^3)(1 + \sin^2\theta)$, where $\cos\theta = \hat{\boldsymbol{\Omega}} \cdot \hat{\boldsymbol{\mu}}$ (Li et al. 2012). (The same spindown model was used in Akgün et al. (2006) for the precession of triaxial stars; Goldreich (1970), Melatos (1999), and Link & Epstein (2001) studied the precession of axisymmetric stars with vacuum dipole spindown, and Melatos (2000) studied the precession of triaxial stars with vacuum dipole spindown.) The angular velocity of rotation is

$$\boldsymbol{\Omega} = L\left(\frac{\hat{\boldsymbol{e}}_1\hat{\ell}_1}{I_1} + \frac{\hat{\boldsymbol{e}}_2\hat{\ell}_2}{I_2} + \frac{\hat{\boldsymbol{e}}_3\hat{\ell}_3}{I_3}\right) = \frac{L}{I_3}\left[\frac{I_3\hat{\boldsymbol{e}}_1\hat{\ell}_1}{I_1} + \frac{I_3\hat{\boldsymbol{e}}_2\hat{\ell}_2}{I_2} + \hat{\boldsymbol{e}}_3\hat{\ell}_3\right] \tag{35}$$

where $I_3 > I_2 > I_1$ are the moments of inertia along the principal axes of the quadrupolar distortion; we define a parameter $0 < e^2 < \infty$, which measures the degree of triaxiality, in terms of which

$$\begin{aligned} &\frac{I_3}{I_2} = 1 + \frac{2\epsilon_{\rm mag}}{2 + e^2}, \qquad \frac{I_3}{I_1} = 1 + \frac{2(1 + e^2)\epsilon_{\rm mag}}{2 + e^2}, \\ &e^2 = \frac{I_3(I_2 - I_1)}{I_1(I_3 - I_2)} \end{aligned} \tag{36}$$

where $\epsilon_{\rm mag}$ is given by Equation (2). *Oblate* axisymmetric distortions ($I_1 = I_2$) correspond to $e^2 = 0$; *prolate* axisymmetric distortions ($I_3 = I_2$) correspond to $e^2 \to \infty$. For the tilted dipole model (see Equation (14) and Lasky & Melatos 2013)

$$e^2 = \frac{I_3(|1 - d|\sqrt{1 + \Delta} + 1 - d)}{I_1(|1 - d|\sqrt{1 + \Delta} - (1 - d))}, \qquad \Delta = \frac{4d\sin^2\sigma}{(1 - d)^2} \,. \tag{37}$$

The principal axes are $(\hat{\boldsymbol{e}}_1, \hat{\boldsymbol{e}}_2, \hat{\boldsymbol{e}}_3) = (\hat{\boldsymbol{e}}_-, \hat{\boldsymbol{v}}, \hat{\boldsymbol{e}}_+)$ according to Equation (16). For $d \gg 1 \Rightarrow \Delta \simeq 4\sin^2\sigma/d \ll 1$ the dipole field dominates the quadrupolar distortion and Equation (37) implies that $e^2 \simeq \Delta/4 \simeq \sin^2\sigma/d \ll 1$. For $d \ll 1 \Rightarrow \Delta \simeq 4d\sin^2\sigma \ll 1$ the toroidal field dominates the quadrupolar distortion, and Equation (37) implies that $e^2 \simeq 4/\Delta = 1/d\sin^2\sigma \gg 1$. For $\sigma = 0$, the axisymmetric case, $e^2 = 0$ if $d > 1$ and $e^2 = \infty$ for $d < 1$. For the numerical examples in Section 3 we adopt $e^2 = 10$, which corresponds to $\Delta \simeq 40/81$ or $d\sin^2\sigma/(1 - d) \simeq 10/81 \approx 0.123$, implying a quadrupolar distortion that is predominantly but not overwhelmingly due to the toroidal field according to Equation (27).

The Euler equations have an exact conservation law

$$\hat{\ell}_1^2 + \hat{\ell}_2^2 + \hat{\ell}_3^2 = 1 \tag{38}$$

because $\hat{\boldsymbol{\ell}}$ is a unit vector, but there is also an approximate conservation law

$$\boldsymbol{\Omega} \cdot \hat{\boldsymbol{\ell}} = \frac{\hat{\ell}_1^2}{I_1} + \frac{\hat{\ell}_2^2}{I_2} + \frac{\hat{\ell}_3^2}{I_3} \equiv \frac{2E_{\rm rot}}{L_0^2} \,; \tag{39}$$

$d^\star(\boldsymbol{\Omega} \cdot \hat{\boldsymbol{\ell}})/dt = -\boldsymbol{\Omega} \cdot \boldsymbol{N}_\perp$ so $\boldsymbol{\Omega} \cdot \hat{\boldsymbol{\ell}}$ only varies appreciably on a timescale of the order of $1/\epsilon_{\rm mag}$ times the spindown time. In Equation (39) the parameter L_0 is the magnitude of the stellar angular momentum at some reference start time, which could be the time when precession is excited.

The Euler equations allow steady-state rotation about any of the three principal axes. By combining Equations (38) and (39) in three different ways appropriate to perturbation away from

each principal axis we find

$$\frac{E_{\rm rot}}{L_0^2/2I_3} - 1 = \frac{2\epsilon_{\rm mag}[\hat{\ell}_1^2(1+e^2)+\hat{\ell}_2^2]}{2+e^2}$$
$$\frac{E_{\rm rot}}{L_0^2/2I_2} - 1 = \frac{2\epsilon_{\rm mag}(\hat{\ell}_1^2 e^2 - \hat{\ell}_3^2)}{2+e^2+2\epsilon_{\rm mag}}$$
$$\frac{E_{\rm rot}}{L_0^2/2I_1} - 1 = -\frac{2\epsilon_{\rm mag}[\hat{\ell}_2^2 e^2 + \hat{\ell}_3^2(1+e^2)]}{2+e^2+2\epsilon_{\rm mag}(1+e^2)}\,. \quad (40)$$

Equation (40) shows that at a given angular momentum, the lowest energy state is a rotation about $\hat{\boldsymbol{e}}_3$, the highest is a rotation about $\hat{\boldsymbol{e}}_1$, and a rotation about $\hat{\boldsymbol{e}}_2$ is intermediate, as is well known. For axisymmetric oblate precession ($e^2 = 0$) the $\hat{\boldsymbol{e}}_1$ and $\hat{\boldsymbol{e}}_2$ directions are interchangeable, and precession is unstable about either one but stable about the symmetry axis $\hat{\boldsymbol{e}}_3$, but for axisymmetric prolate precession ($e^2 \to \infty$) the $\hat{\boldsymbol{e}}_2$ and $\hat{\boldsymbol{e}}_3$ directions are interchangeable, and precession is stable about either one and unstable about the symmetry axis $\hat{\boldsymbol{e}}_1$.

Below, we will use the first part of Equation (40) to quantify the second conservation law by defining the energy perturbation above the minimum energy state to be

$$E_{\rm rot} = \frac{L_0^2}{2I_3}\left[1 + \frac{2\epsilon_{\rm mag}\Lambda^2(1+e^2)}{2+e^2}\right]$$
$$\Rightarrow \delta E_p = E_{\rm rot} - \frac{L_0^2}{2I_3} = \frac{L_0^2\Lambda^2\epsilon_{\rm mag}(1+e^2)}{I_3(2+e^2)}\,, \quad (41)$$

where δE_p is the extra energy associated with precession. Using Equation (41) we write the conservation law as

$$\Lambda^2(1+e^2) = \hat{\ell}_1^2(1+e^2) + \hat{\ell}_2^2\,. \quad (42)$$

Suppose precession is excited from its minimum energy state by injection of rotational energy $\delta E_p = \eta L_0^2/2I_3$. This is consistent with exciting precession with amplitude

$$\Lambda^2(1+e^2) = \frac{(2+e^2)\eta}{2\epsilon_{\rm mag}} \equiv \frac{\eta}{\eta_{\rm crit}} \qquad \eta_{\rm crit} = \frac{2\epsilon_{\rm mag}}{2+e^2}\,. \quad (43)$$

There are then two very different cases depending on how much energy is injected: if $\eta < \eta_{\rm crit}$ then $\Lambda^2(1+e^2) < 1$ and if $\eta > \eta_{\rm crit}$ then $\Lambda^2(1+e^2) > 1$. We shall treat each of these cases, which have very different properties, separately. Qualitatively, we shall see that $\Lambda^2(1+e^2) < 1$ has well-defined $e^2 \to 0$ (axisymmetric, oblate) limiting dynamics whereas $\Lambda^2(1+e^2) > 1$ has well-defined $e^2 \to \infty$ (axisymmetric, prolate) limiting dynamics. Since

$$\epsilon_{\rm mag} \simeq \frac{\beta_2 E_{\rm mag}}{E_\star} \quad (44)$$

where $E_{\rm mag} \sim B^2R^3$ is the magnetic energy and $E_\star \sim GM^2/R$ is the binding energy of the neutron star, a more apt comparison is

$$\frac{\delta E_p}{E_{\rm mag}} \simeq \frac{2\beta_2\epsilon_{\rm rot}(1+e^2)\Lambda^2}{2+e^2} \quad (45)$$

where $\epsilon_{\rm rot} = L^2/2I_3E_\star$ is the rotational distortion of the star. This separation into two regimes does not appear to have been emphasized in previous astrophysics literature on triaxial precession, although no doubt Euler was well aware of it.

For a rotation period $\sim$1 s we expect $\epsilon_{\rm rot} \sim I\Omega^2R/GM^2 \sim 10^{-7}I_{45}R_{10}^3/M_{1.4}[P\,({\rm s})]^2$ so the energy required to excite even high-amplitude precession is only a small fraction of the magnetic energy of the star. Even small changes in the magnetic field can engender relatively large amplitude precession. To make this quantitative, suppose that a shearing event in the neutron star distorts the magnetic field changing the moment of inertia of the star from $\boldsymbol{I}$ to $\boldsymbol{I}' = \boldsymbol{I} + \Delta\boldsymbol{I}$, where $\Delta\boldsymbol{I}$ is STF. The eigenvalues of $\boldsymbol{I}'$ are slightly different from those of $\boldsymbol{I}$, and its eigenvectors are rotated relative to the eigenvectors of $\boldsymbol{I}$. If the eigenvalues and associated eigenvectors of $\boldsymbol{I}$ are $(I_i, \hat{\boldsymbol{e}}_i)$, then to lowest order in $||\Delta\boldsymbol{I}||$ the eigenvalues and eigenvectors of $\boldsymbol{I}'$ are

$$I_i' = I_i + \Delta I_{ii}$$
$$\hat{\boldsymbol{e}}_i' \simeq \hat{\boldsymbol{e}}_i\left(1 - \tfrac{1}{2}\sum_{j\neq i}\theta_{ij}^2\right) + \sum_{j\neq i}\theta_{ij}\hat{\boldsymbol{e}}_j$$
$$\theta_{ij} = \frac{\Delta I_{ij}}{I_i' - I_j'}\,, \quad (46)$$

normalizing the eigenvectors so that $\hat{\boldsymbol{e}}_i'\cdot\hat{\boldsymbol{e}}_j' = \delta_{ij}$. Since we expect $\Delta I_{ij} = s_{ij}\epsilon_{\rm mag}$, where s_{ij} is STF with magnitude $\lesssim 1$, and $|I_i' - I_j'| \sim \epsilon_{\rm mag}$ the rotations involve angles $\lesssim 1$, not $\sim\epsilon_{\rm mag} \ll 1$. Assuming that $\boldsymbol{L}$ is conserved in the shearing event, its projection along the rotated principal axes of $\boldsymbol{I}'$ differs from its projection along $\boldsymbol{I}$. For example, suppose that the star was rotating without any precession at all along $\hat{\boldsymbol{e}}_3$, the axis of the largest moment of inertia, prior to the shearing event; then afterward

$$\hat{\boldsymbol{\ell}} \simeq \hat{\boldsymbol{e}}_1'\theta_{13} + \hat{\boldsymbol{e}}_2'\theta_{23} + \hat{\boldsymbol{e}}_3'\left[1 - \tfrac{1}{2}(\theta_{13}^2 + \theta_{23}^2)\right]\,, \quad (47)$$

and the star will precess. If angular momentum is conserved as the field rearranges itself, then the angular velocity changes during the shearing event by

$$\Delta\Omega_i = -\frac{\Delta I_{ij}\Omega_j}{I_i}$$

working in the reference frame where $\boldsymbol{I}$ is diagonal. The associated change in rotational energy is

$$\Delta E_{\rm rot} = L_i\Delta\Omega_i = -\frac{L_i\Delta I_{ij}\Omega_j}{I_i} = -\Omega_i\Delta I_{ij}\Omega_j$$
$$= -\epsilon_{\rm mag}\Omega_i s_{ij}\Omega_j\,. \quad (48)$$

$\Delta E_{\rm rot}$ might be negative or positive, and is not equal to the extra energy in precession above the minimum energy state corresponding to rotation about $\hat{\boldsymbol{e}}_3'$, in part because the magnitude of the angular velocity changes as a result of the shearing event. In rough order of magnitude $|\delta E_{\rm rot}| \lesssim \epsilon_{\rm rot}E_{\rm mag}$.

Phenomena associated with the spindown torque include a cyclical variation over a precession cycle and a secular torque that develops very slowly compared with the precession period. We discuss these in Sections 2.4 and 2.5 using a perturbative technique similar to that of Goldreich (1970) but generalized to triaxial precession. To zeroth order, we neglect spindown

effects, and Equation (33) becomes

$$\frac{d\hat{\boldsymbol{\ell}}_1}{d\phi} = -\frac{2\epsilon_{\rm mag}\hat{\boldsymbol{\ell}}_2\hat{\boldsymbol{\ell}}_3}{2+e^2} \quad \frac{d\hat{\boldsymbol{\ell}}_2}{d\phi} = \frac{2\epsilon_{\rm mag}\hat{\boldsymbol{\ell}}_1\hat{\boldsymbol{\ell}}_3(1+e^2)}{2+e^2}$$
$$\frac{d\hat{\boldsymbol{\ell}}_3}{d\phi} = -\frac{2\epsilon_{\rm mag}\hat{\boldsymbol{\ell}}_1\hat{\boldsymbol{\ell}}_2 e^2}{2+e^2} \tag{49}$$

where $d\phi = (L/I_3)dt$ is the differential spin phase.

From an observational standpoint, we are most interested in the motion of the direction from the star to the observer, $\hat{\boldsymbol{n}}$, in the rotating frame of reference. In the inertial frame, where $\hat{\boldsymbol{\ell}}$ is independent of time to lowest order, let

$$\hat{\boldsymbol{n}} = \cos i\hat{\boldsymbol{\ell}} + \sin i\hat{\boldsymbol{e}}_x \,. \tag{50}$$

To project $\hat{\boldsymbol{n}}$ onto the rotating frame we use a standard Euler angle rotation (e.g., Gottfried 1966, Figure 32.1): (i) Rotate angle $\alpha \in [0,\ 2\pi]$ about the 3 axis to get new axes $1'$, $2'$, $3' = 3$. (ii) Rotate angle $\beta \in [0,\ \pi]$ about the $2'$ axis to get new axes $1''$, $2'' = 2'$, $3'' = z$. (iii) Rotate angle $\gamma \in [0,\ 2\pi]$ about the $3'' = z$ axis to get the axes x, y, z. In terms of the angles α, β, and γ we get $\hat{\boldsymbol{n}} = \hat{n}_i\hat{\boldsymbol{e}}_i$, where

$$\hat{n}_1 = \sin i(\cos\alpha\cos\beta\cos\gamma - \sin\alpha\sin\gamma) - \cos i\cos\alpha\sin\beta$$
$$\hat{n}_2 = \sin i(\sin\alpha\cos\beta\cos\gamma + \cos\alpha\sin\gamma) - \cos i\sin\alpha\sin\beta$$
$$\hat{n}_3 = \sin i\cos\gamma\sin\beta + \cos i\cos\beta. \tag{51}$$

If we define $\hat{\boldsymbol{\ell}} = \hat{\boldsymbol{z}}$ in the inertial frame we find that $\cos\beta = \hat{\boldsymbol{\ell}}_3$ and

$$\sin\alpha = -\frac{\hat{\boldsymbol{\ell}}_2}{\sqrt{\hat{\boldsymbol{\ell}}_1^2 + \hat{\boldsymbol{\ell}}_2^2}} \qquad \cos\alpha = -\frac{\hat{\boldsymbol{\ell}}_1}{\sqrt{\hat{\boldsymbol{\ell}}_1^2 + \hat{\boldsymbol{\ell}}_2^2}} \,. \tag{52}$$

Using $d\hat{\boldsymbol{e}}_i/dt = \boldsymbol{\Omega} \times \hat{\boldsymbol{e}}_i$ for any of the principal axes we find that

$$\frac{d\gamma}{d\phi} = -1 - \frac{2\epsilon_{\rm mag}[(1+e^2)\hat{\boldsymbol{\ell}}_1^2 + \hat{\boldsymbol{\ell}}_2^2]}{(2+e^2)(\hat{\boldsymbol{\ell}}_1^2 + \hat{\boldsymbol{\ell}}_2^2)}$$
$$= -1 - \frac{2\epsilon_{\rm mag}\Lambda^2(1+e^2)}{(2+e^2)(\hat{\boldsymbol{\ell}}_1^2 + \hat{\boldsymbol{\ell}}_2^2)} \tag{53}$$

using Equation (42). Note that these results can be used for both $\Lambda\sqrt{1+e^2} < 1$ and $\Lambda\sqrt{1+e^2} > 1$.

In the rotating frame of reference, $\hat{\boldsymbol{n}} = \cos i\hat{\boldsymbol{\ell}} + \sin i(\hat{\boldsymbol{e}}_a\cos\gamma + \hat{\boldsymbol{e}}_b\sin\gamma)$, where $\hat{\boldsymbol{e}}_a = (\hat{\boldsymbol{\ell}} \times \hat{\boldsymbol{e}}_3) \times \hat{\boldsymbol{\ell}}/\sin\beta$ and $\hat{\boldsymbol{e}}_b = \hat{\boldsymbol{\ell}} \times \hat{\boldsymbol{e}}_3/\sin\beta$ are slowly varying unit vectors perpendicular to $\hat{\boldsymbol{\ell}}$; $\hat{\boldsymbol{n}}$ rotates rapidly in the retrograde direction in the plane instantaneously perpendicular to $\hat{\boldsymbol{\ell}}$. For emission along a beam direction $\hat{\boldsymbol{b}}$ the observed intensity depends on $\hat{\boldsymbol{b}}\cdot\hat{\boldsymbol{n}} = \cos i\hat{\boldsymbol{b}}\cdot\hat{\boldsymbol{\ell}} + \sin i(\hat{\boldsymbol{b}}\cdot\hat{\boldsymbol{e}}_a\cos\gamma + \hat{\boldsymbol{b}}\cdot\hat{\boldsymbol{e}}_b\sin\gamma)$. Define $\hat{\boldsymbol{b}}\cdot\hat{\boldsymbol{\ell}} = \cos\eta_b$, $\hat{\boldsymbol{b}}\cdot\hat{\boldsymbol{e}}_a = \sin\eta_b\cos\psi_b$, and $\hat{\boldsymbol{b}}\cdot\hat{\boldsymbol{e}}_b = \sin\eta_b\sin\psi_b$; then

$$\hat{\boldsymbol{b}}\cdot\hat{\boldsymbol{n}} = \cos i\cos\eta_b + \sin i\sin\eta_b\cos(\gamma - \psi_b) \,, \tag{54}$$

where η_b and ψ_b vary during the precession cycle for a given $\hat{\boldsymbol{b}}$.

For "pulsar-like" behavior, beam directions are randomly distributed in a narrow cone around a dominant direction. Given unlimited sensitivity, the observed intensity would be nearly periodic, with periodic timing residuals due to precession $\lesssim 1$ rad of spin phase. The amplitude of the rapidly oscillating term in Equation (54) is $\propto \sin\eta_b$, which varies during the precession cycle. Presumably the observed intensity is a decreasing function of $\hat{\boldsymbol{b}}\cdot\hat{\boldsymbol{n}}$, so the observed intensity has extrema when

$$\frac{d\hat{\boldsymbol{b}}\cdot\hat{\boldsymbol{n}}}{d\phi} = 0 \,, \tag{55}$$

which has solutions twice per cycle, only one of which corresponds to the maximum value of $\hat{\boldsymbol{b}}\cdot\hat{\boldsymbol{n}}$. (Our method of solution and solutions of Equation (55) are presented in Cordes et al. 2021.) Intrinsic intensity fluctuations and imperfect, time-varying, and often unfavorable beaming due to precession turn out to render most pulses undetectable, but nevertheless the spin frequency would be readily discernible in this case.

For "stochastic" behavior, in which outbursts occur randomly in time with a random distribution of beam directions, it is much harder but not impossible to uncover the pulse frequency. If the beams emit into narrow cones, Equation (54) implies that most outbursts will not be seen but there will be a bias favoring times when $\hat{\boldsymbol{b}}\cdot\hat{\boldsymbol{n}}$ is near one. This bias imprints the effect of fast rotation on the times when outbursts happen, but only weakly, so the spin frequency is only discernible after many bursts have been detected. We develop a specific model for stochastic outbursts in Section 3. An approximate analytic model that elucidates how information about the spin frequency and precession period is imprinted on the modeled series of burst detection times may be found in Appendix B.

Intermediate between these two extreme models would be one in which FRBs occur randomly in time but are triggered by exceptionally narrow beams within a restricted range of possible directions. For an outburst occurring at a particular time, the associated FRB would only be seen if $\hat{\boldsymbol{b}}$ is very nearly parallel to $\hat{\boldsymbol{n}}$, as determined from Equation (51) with Equation (52), *and* $\hat{\boldsymbol{n}}$ is in the range of allowed beam directions.

Table 1 details the solutions of the Euler equations. Note that the solutions are continuous across the limiting case $\Lambda\sqrt{1+e^2} = 1 = q$, but because the precession period diverges logarithmically as $q \to 1$ (from either side) the solutions are not really connected physically across $q = 1$. Figure 1 depicts the solutions for $\Lambda = 0.2$ and $e^2 = 10$. The left panel shows the motion of $\hat{\boldsymbol{\ell}}$ in three dimensions (arrows) and its projection onto the $1-2$ plane (green points), which is the ellipse given by Equation (42). The right panel shows the projection onto the $1-3$ plane. In both panels the black arrows indicate the principal axes, the blue arrow indicates the direction of $\hat{\boldsymbol{t}}$, and the red arrow indicates the direction of $\hat{\boldsymbol{\mu}}$; ζ is the angle between $\hat{\boldsymbol{t}}$ and $\hat{\boldsymbol{e}}_1 = \hat{\boldsymbol{e}}_-$ and σ is the angle between $\hat{\boldsymbol{\mu}}$ and $\hat{\boldsymbol{t}}$ defined in Equation (13).

There are two different axisymmetric situations, $e^2 = 0$, which is oblate ($I_1 = I_2 < I_3$), and $e^2 = \infty$, which is prolate ($I_3 = I_2 > I_1$); these solutions are listed in Table 1. However, these are singular limiting cases: $q = e\Lambda/\sqrt{1-\Lambda^2}$ is identically zero for $e = 0$ for any value of $\Lambda \neq 1$ and is infinity for $e = \infty$ for any value of $\Lambda \neq 0$.

The ratio of the neutron star's spin period P to its precession period P_p is

$$\frac{P}{P_p} = \frac{2\pi}{\phi_{p,\rm cyc}} = \frac{\pi\epsilon_{\rm mag}e\Lambda\sqrt{1+e^2}}{2+e^2}\begin{cases} 1/qF(\pi/2|q) & [q<1] \\ 1/F(\pi/2|1/q) & [q>1] \end{cases} \tag{56}$$

Table 1
Precession Solutions

	$0 < \Lambda\sqrt{1+e^2} < 1$	$1 < \Lambda\sqrt{1+e^2} < \sqrt{1+e^2}$ [a]
q	$\frac{e\Lambda}{\sqrt{1-\Lambda^2}} < 1$	$\frac{e\Lambda}{\sqrt{1-\Lambda^2}} > 1$
Φ [b]	$F(\varphi(\Phi)\vert q) = \int_0^{\varphi(\Phi)} \frac{d\varphi'}{\sqrt{1-q^2\sin^2\varphi'}}$	$F(\varphi(\Phi)\vert 1/q) = \int_0^{\varphi(\Phi)} \frac{d\varphi'}{\sqrt{1-\sin^2\varphi'/q^2}}$
$\mathrm{sn}\,\Phi$	$\sin[\varphi(\Phi)]$	$\sin[\varphi(\Phi)]$
$\mathrm{cn}\,\Phi$	$\cos[\varphi(\Phi)]$	$\cos[\varphi(\Phi)]$
$\mathrm{dn}\,\Phi$	$\sqrt{1-q^2\,\mathrm{sn}^2\,\Phi}$	$\sqrt{1-\mathrm{sn}^2\,\Phi/q^2}$
$\Phi_{p,\mathrm{cyc}}$ [c]	$4F(\pi/2\vert q)$	$4F(\pi/2\vert 1/q)$
$d\Phi/d\phi$	$\frac{2\epsilon_{\mathrm{mag}}\sqrt{(1-\Lambda^2)(1+e^2)}}{2+e^2} = \frac{2\epsilon_{\mathrm{mag}}e\Lambda\sqrt{1+e^2}}{q(2+e^2)}$	$\frac{2\epsilon_{\mathrm{mag}}e\Lambda\sqrt{1+e^2}}{2+e^2} = \frac{2\epsilon_{\mathrm{mag}}q\sqrt{(1-\Lambda^2)(1+e^2)}}{2+e^2}$
$\phi_{p,\mathrm{cyc}}$ [d]	$\frac{2(2+e^2)F(\pi/2\,\vert\,q)}{\epsilon_{\mathrm{mag}}\sqrt{(1-\Lambda^2)(1+e^2)}} = \frac{2q(2+e^2)F(\pi/2\,\vert\,q)}{\epsilon_{\mathrm{mag}}e\Lambda\sqrt{1+e^2}}$	$\frac{2(2+e^2)F(\pi/2\,\vert\,1/q)}{\epsilon_{\mathrm{mag}}e\Lambda\sqrt{1+e^2}} = \frac{2(2+e^2)F(\pi/2\,\vert\,1/q)}{\epsilon_{\mathrm{mag}}q\sqrt{(1-\Lambda^2)(1+e^2)}}$
$\hat{\ell}_1$	$\Lambda\,\mathrm{cn}\,\Phi$	$\Lambda\,\mathrm{dn}\,\Phi$
$\hat{\ell}_2$	$\Lambda\sqrt{1+e^2}\,\mathrm{sn}\,\Phi$	$\frac{\sqrt{(1-\Lambda^2)(1+e^2)}\,\mathrm{sn}\,\Phi}{e} = \frac{\Lambda\sqrt{1+e^2}\,\mathrm{sn}\,\Phi}{q}$
$\hat{\ell}_3$	$\sqrt{1-\Lambda^2}\,\mathrm{dn}\,\Phi$	$\sqrt{1-\Lambda^2}\,\mathrm{cn}\,\Phi$
$1+\frac{d\gamma}{d\phi}$	$-\frac{\sqrt{1+e^2}\,d\Phi/d\phi}{\sqrt{(1-\Lambda^2)(1+e^2\,\mathrm{sn}^2\,\Phi)}} = -\frac{q\sqrt{1+e^2}\,d\Phi/d\phi}{e\Lambda(1+e^2\,\mathrm{sn}^2\,\phi)}$	$-\frac{\Lambda\sqrt{1+e^2}\,d\Phi/d\phi}{e[\Lambda^2+(1-\Lambda^2)\,\mathrm{sn}^2\,\Phi]} = -\frac{\sqrt{1+e^2}\,d\Phi/d\phi}{e\Lambda(1+e^2\,\mathrm{sn}^2\,\Phi/q^2)}$ $= -\frac{\sqrt{1+e^2}\,d\Phi/d\phi}{q\sqrt{1-\Lambda^2}(1+e^2\,\mathrm{sn}^2\,\Phi/q^2)}$

	$e^2 = 0.0$ (Axisymmetric, Oblate)	$e^2 = \infty$ (Axisymmetric, Prolate)
$d\Phi/d\phi$	$\epsilon_{\mathrm{mag}}\sqrt{1-\Lambda^2}$	$2\epsilon_{\mathrm{mag}}\Lambda$
$\hat{\ell}_1$	$\Lambda\cos\Phi$	Λ
$\hat{\ell}_2$	$\Lambda\sin\Phi$	$\sqrt{1-\Lambda^2}\,\sin\Phi$
$\hat{\ell}_3$	$\sqrt{1-\Lambda^2}$	$\sqrt{1-\Lambda^2}\,\cos\Phi$
$1+\frac{d\gamma}{d\phi}$	$-\frac{d\Phi/d\phi}{\sqrt{1-\Lambda^2}} = -\epsilon_{\mathrm{mag}}$	$-\frac{2\epsilon_{\mathrm{mag}}\Lambda^2}{\Lambda^2+(1-\Lambda^2)\sin^2\Phi}$

Notes.
[a] $\Lambda < 1$ is required.
[b] Precession phase. $F(\varphi|q)$ and $F(\varphi|1/q)$ are elliptic functions (e.g., Abramowitz & Stegun 1972).
[c] Precession phase per precession cycle.
[d] Spin phase per precession cycle.

which is plotted in Figure 2 for various values of e^2 as a function of $\Lambda\sqrt{1+e^2}$. The smallest values of $P/P_p\epsilon_{\mathrm{mag}}$ are for $\Lambda\sqrt{1+e^2} < 1$ and large e^2, except for the region right around $\Lambda\sqrt{1+e^2} = 1$, where $P/\epsilon_{\mathrm{mag}}P_p \to 0$ for all values of e^2. Since FRB 121102 and FRB 180916.J0158+65 both have very long P_p, Figure 2 favors models with large values of e^2, which implies that the toroidal component of the magnetic field is significantly larger than the poloidal component, unless the star is fortuitously close to $\Lambda\sqrt{1+e^2} = 1$.

2.4. Periodic Timing Residuals from Precession plus Spindown

Here, we derive the equation for $t(\phi)$, the functional dependence of time on spin phase, which we have defined previously as $d\phi = (L/I_3)dt$; we use Equations (32) and (34) to *zeroth order* in ϵ_{mag} to get

$$\frac{d\Omega}{d\phi} = -\frac{k\mu^2\Omega^2[1-a(\hat{\boldsymbol{\mu}}\cdot\hat{\boldsymbol{\ell}})^2]}{Ic^3}$$
$$\Rightarrow \frac{d}{d\phi}\left(\frac{1}{\Omega}\right) = \frac{d^2t}{d\phi^2} = \frac{k\mu^2[1-a(\hat{\boldsymbol{\mu}}\cdot\hat{\boldsymbol{\ell}})^2]}{Ic^3} \tag{57}$$

where $dt/d\phi = 1/\Omega$ and $I_i \simeq I$ in this approximation. The solution to Equation (57) is a continuous function $t(\phi)$ that exhibits the timing residuals due to spindown; for a single beam, which is appropriate for a precessing pulsar, we evaluate at $\{\phi_i\}$, the discrete set of spin phases where the pulses are beamed toward the observer optimally.

The dependence on precession phase arises from

$$[\hat{\boldsymbol{\mu}}\cdot\hat{\boldsymbol{\ell}}\,(\Phi)]^2 = \sum_i \hat{\mu}_i^2\hat{\ell}_i^2 + 2\sum_{i\neq j}\hat{\mu}_i\hat{\mu}_j\hat{\ell}_i\hat{\ell}_j$$
$$= \hat{\boldsymbol{\mu}}_1^2\Lambda^2 + \hat{\boldsymbol{\mu}}_3^2(1-\Lambda^2) + \hat{\boldsymbol{\ell}}_2^2\left(-\frac{\hat{\mu}_1^2+\hat{\mu}_3^2e^2}{1+e^2} + \hat{\boldsymbol{\mu}}_2^2\right)$$
$$+ 2\sum_{i\neq j}\hat{\mu}_i\hat{\mu}_j\hat{\ell}_i\hat{\ell}_j\,, \tag{58}$$

where we use the conservation laws, Equations (38) and (42), to separate out the constant term and isolate the dependence on $\hat{\boldsymbol{\ell}}_2^2 \propto \mathrm{sn}^2\,\Phi$. In evaluating $t(\phi)$ we must be careful to isolate secularly growing terms from terms that are periodic over a precession cycle. We write the solution to Equation (57) succinctly as

$$t(\phi) = t(0) + \frac{\phi}{\Omega(0)}\left[1 - \frac{2ak\mu^2\Omega(0)}{Ic^3(d\Phi/d\phi)}\sum_{i<j}\hat{\mu}_i\hat{\mu}_jC_{ij}\right]$$
$$+ \frac{k\mu^2\phi^2}{2Ic^3}\left\{1 - a[\hat{\boldsymbol{\mu}}_1^2\Lambda^2 + \hat{\boldsymbol{\mu}}_3^2(1-\Lambda^2)\right.$$
$$\left. + \langle\hat{\boldsymbol{\ell}}_2^2\rangle\left(-\frac{\hat{\mu}_1^2+\hat{\mu}_3^2e^2}{1+e^2} + \hat{\boldsymbol{\mu}}_2^2\right)\right]\right\}$$
$$- \frac{ak\mu^2}{Ic^3(d\Phi/d\phi)^2}\left[\left(\hat{\boldsymbol{\mu}}_2^2 - \frac{\hat{\mu}_1^2+\hat{\mu}_3^2e^2}{1+e^2}\right)P_{22}(\Phi) + 2\sum_{ij}\hat{\mu}_i\hat{\mu}_jP_{ij}(\Phi)\right], \tag{59}$$

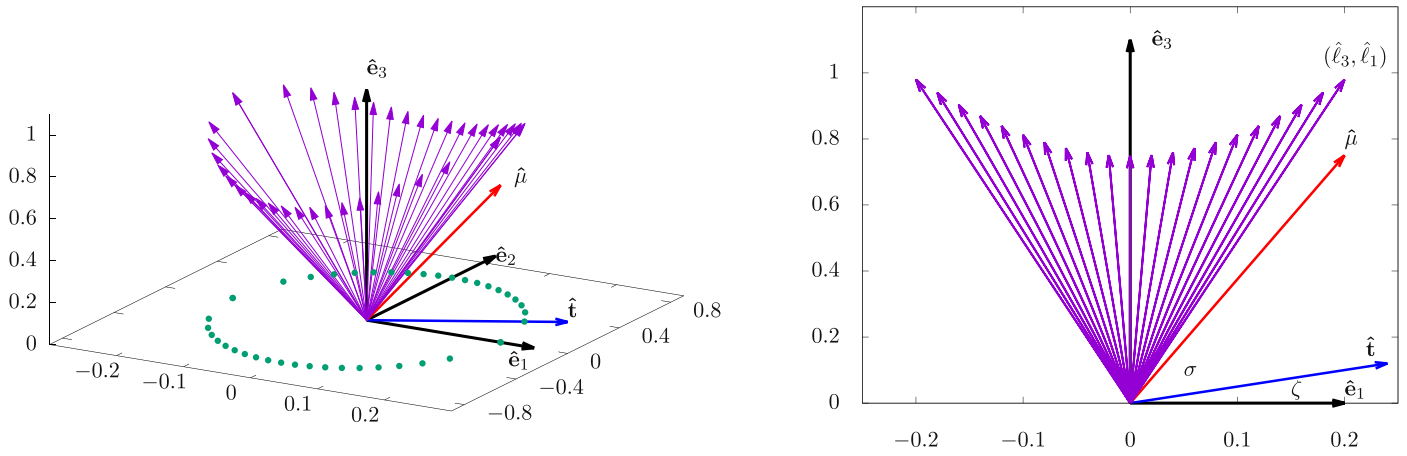

Figure 1. Solution for $\hat{\ell}$ with $\Lambda = 0.2$ and $e^2 = 10$. Left: 3D motion of $\hat{\ell}$ (arrows) and projection onto 1–2 plane (green points). Right: Projection onto 1–3 plane. In both panels, the black arrows denote the principal axes, and the blue and red arrows are the directions of $\hat{\boldsymbol{t}}$ and $\hat{\boldsymbol{\mu}}$, respectively. The symbols ζ and σ are the angles between $\hat{\boldsymbol{t}}$ and $\hat{\boldsymbol{e}}_1$ and $\hat{\boldsymbol{\mu}}$, respectively.

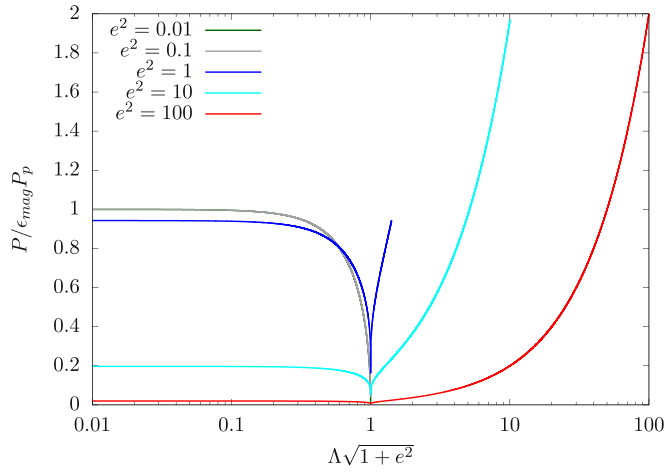

Figure 2. $P/\epsilon_{\rm mag}P_p$ as a function of $\Lambda\sqrt{1+e^2}$ for $e^2 = 0.01$, 0.1, 1, 10, and 100.

where $1/\Omega(0) = (dt/d\phi)_0$. The coefficients in Equation (59) are given in Table 2. The various averages and functions in Table 2 are evaluated in Appendix A.

For calculations, it is convenient to express $t - t(0)$ in terms of the precession period P_p. Then $\phi/\Omega(0)P_p = \Phi/\Phi_{p,\rm cycle}$ and the remaining terms all depend on the single nondimensional parameter

$$\epsilon_{\rm sd} = \frac{\mu^2\Omega^2(0)P_p}{I_0 c^3} = \frac{P_p}{t_{\rm sd}} \simeq \frac{2.3\times 10^{-4}B_{D,14}^2 R_{10}^4 (P_p/100\ {\rm days})}{[P({\rm s})]^2 M_{1.4}(I_0/0.2MR^2)} \tag{60}$$

because Equation (57) may be written in the form

$$\frac{d^2(t/P_p)}{d\Phi^2} = \frac{k\epsilon_{\rm sd}[1 - a(\hat{\boldsymbol{\mu}}\cdot\hat{\boldsymbol{\ell}})^2]}{\Phi^2_{p,\rm cycle}} \ .$$

From Equation (59) we see that in addition to the apparent frequency shift $\mathcal{O}(\epsilon_{\rm mag})$ arising from precession there is another apparent frequency shift $\mathcal{O}(\epsilon_{\rm sd})$.

The amplitude of the cyclical terms is of the order of

$$\Delta t_{\rm sd,\ cyc} = \epsilon_{\rm sd}P_p = \frac{P_p^2}{t_{\rm sd}} \tag{61}$$

and the cyclical shift in pulse phase due to spindown is of the order of

$$\Omega(0)\,\Delta t_{\rm sd,\ cyc} = \frac{2\pi\epsilon_{\rm sd}P_p}{P} = \frac{2\pi P_p^2}{P t_{\rm sd}} \tag{62}$$

which can be large for

$$\epsilon_{\rm sd} \gtrsim \epsilon_{\rm sd,1} \equiv \frac{P}{P_p} \sim \epsilon_{\rm mag} \tag{63}$$

(Cordes 1993). The secular terms $\propto \Phi^2$ also become progressively more important for $\epsilon_{\rm sd} > \epsilon_{\rm sd,1}$ and, if large enough, may frustrate searches for the underlying spin period of the precessing magnetar in models based on stochastic outbursts. Equations (60) and (63) imply that

$$\frac{\epsilon_{\rm sd}}{\epsilon_{\rm sd,1}} = \frac{\mu^2\Omega^2(0)P_p^2}{I_0 c^3 P} = \frac{1.9\times 10^3 B_{D,14}^2 R_{10}^4 (P_p/100\ {\rm days})^2}{[P({\rm s})]^3 M_{1.4}(I_0/0.2MR^2)} \tag{64}$$

which is between $\sim 5B_{D,14}^2$ and $\sim 5000B_{D,14}^2$ if $P_p = 160$ days (FRB 121102) and between $\sim 0.05B_{D,14}^2$ and $\sim 50B_{D,14}^2$ if $P_p = 16.4$ days (FRB 180916.J0158+65) for $1/P \sim 0.1-1\ {\rm s}^{-1}$.

2.5. Secular Evolution of Precession via $\boldsymbol{N}_\perp$

We now consider how precession evolves as a consequence of spindown, generalizing Goldreich (1970) to cases with $e^2 \neq 0$. As in Goldreich (1970) we consider effects to lowest order in $\epsilon_{\rm mag}$. We generalize the solutions to the Euler equations to include a slow evolution of the amplitude parameter $\Lambda = \Lambda(\epsilon t)$, as was done by Goldreich (1970), but also include a slowly varying phase shift by replacing $\Phi = (d\Phi/d\phi)\phi$ with $\tilde{\Phi}(t) = \Phi + \psi(\epsilon t)$. This phase shift is required for triaxial precession evolving via spindown. Here $\epsilon = ak\mu^2(L/I_3)^2/c^3 I_3$ is roughly the inverse spindown time. We assume that the spindown time is long compared with the precession timescale, a necessary condition for a perturbative treatment; this assumption fails at early times, or if $\Lambda\sqrt{1+e^2} \to 1$.

Table 2
Coefficients in Timing Model

	$q<1$	$q>1$
$\langle \hat{\ell}_2^2 \rangle$	$\Lambda^2(1+e^2)\langle \mathrm{sn}^2\Phi\rangle$	$(1-\Lambda^2)(1+1/e^2)\langle \mathrm{sn}^2\Phi\rangle$
C_{12}	$\frac{\Lambda^2\sqrt{1+e^2}(1-\langle \mathrm{dn}\,\Phi\rangle)}{q^2}$	$\Lambda\sqrt{(1-\Lambda^2)(1+1/e^2)}$
C_{13}	0	0
C_{23}	$\Lambda\sqrt{(1-\Lambda^2)(1+e^2)}$	$q^2(1-\Lambda^2)\sqrt{1+1/e^2}(1-\langle \mathrm{dn}\,\Phi\rangle)$
P_{12}	$\Lambda^2\sqrt{1+e^2}\,C_2(\Phi\vert q)$	$-\Lambda\sqrt{(1-\Lambda^2)(1+1/e^2)}\,C_4(\Phi\vert 1/q)$
P_{13}	$\Lambda\sqrt{1-\Lambda^2}\,C_3(\Phi\vert q)$	$\Lambda\sqrt{1-\Lambda^2}\,C_3(\Phi\vert 1/q)$
P_{23}	$-\Lambda\sqrt{(1-\Lambda^2)(1+e^2)}\,C_4(\Phi\vert q)$	$(1-\Lambda^2)\sqrt{1+1/e^2}\,C_2(\Phi\vert 1/q)$
P_{22}	$\Lambda^2(1+e^2)C_1(\Phi\vert q)$	$(1-\Lambda^2)(1+1/e^2)C_1(\Phi\vert 1/q)$

We start by considering $\Lambda\sqrt{1+e^2}<1$, which is favored for long precession periods, and is the expected state if precession is excited from rotation about $\hat{\boldsymbol{e}}_3$ with relatively low δE_p. Averaging over the precession phase we find

$$\frac{1}{q}\frac{dq}{dt}=\frac{ak\mu^2(L/I_3)^2}{c^3 I_3}\{\hat{\boldsymbol{\mu}}_1^{\,2}[2-(1+q^2)\langle \mathrm{sn}^2\Phi\rangle] + \hat{\boldsymbol{\mu}}_2^{\,2}[1+(1-2q^2)\langle \mathrm{sn}^2\Phi\rangle]-(1-q^2\langle \mathrm{sn}^2\Phi\rangle)\}$$
$$\frac{d\psi}{dt}=\frac{ak\mu^2(L/I_3)^2\hat{\boldsymbol{\mu}}_1\hat{\boldsymbol{\mu}}_2}{c^3 I_3\sqrt{1+e^2}}\left[\left\langle\frac{\mathrm{cn}^2\Phi}{\mathrm{dn}\,\Phi}\right\rangle-(1+e^2)\left\langle\frac{\mathrm{sn}^2\Phi}{\mathrm{dn}\,\Phi}\right\rangle\right] \tag{65}$$

where we use

$$\frac{dq}{q}=\frac{d\Lambda}{\Lambda}-\frac{d\sqrt{1-\Lambda^2}}{\sqrt{1-\Lambda^2}}=\frac{d\Lambda}{\Lambda}+\frac{\Lambda d\Lambda}{1-\Lambda^2} =\frac{d\Lambda}{\Lambda(1-\Lambda^2)}-\frac{d\sqrt{1-\Lambda^2}}{\Lambda^2\sqrt{1-\Lambda^2}}\,. \tag{66}$$

Equation (65) reduces to the results in Goldreich (1970) for $e^2=0$, the axisymmetric oblate case, for which $\langle \mathrm{cn}^2\Phi\rangle=\langle \mathrm{sn}^2\Phi\rangle=\frac{1}{2}$ and $\mathrm{dn}\,\Phi=1$, after replacing $dq/q\to d\Lambda/\Lambda(1-\Lambda^2)$ using Equation (66); for that case, there is no phase shift ψ. The stability condition implied by the first part of Equation (65) is more complicated than what was found by Goldreich (1970) for the axisymmetric oblate case: there is a separatrix that is an ellipse in the $\hat{\boldsymbol{\mu}}_1-\hat{\boldsymbol{\mu}}_2$ plane whose axes depend on q, so that, for given values of e^2 and $\hat{\boldsymbol{\mu}}_1^{\,2}$ and $\hat{\boldsymbol{\mu}}_2^{\,2}$, there is a fixed point at a specific value of q.

By contrast, for the axisymmetric oblate case, the ellipse degenerates into a circle

$$\hat{\boldsymbol{\mu}}_1^{\,2}+\hat{\boldsymbol{\mu}}_2^{\,2}=\frac{2}{3} \tag{67}$$

irrespective of the value of Λ. In this case, Λ grows as long as the magnetic moment configuration of the star is outside this circle. The growth halts once $\Lambda\to 1$, where $d\Lambda/dt$ also goes to zero. Inside the circle, Λ decreases, reaching $\Lambda=0$ asymptotically.

For the triaxial case q cannot grow beyond $q=1$; since $\langle \mathrm{sn}^2\Phi\rangle=1$ for $q=1$, Equation (65) implies $dq/dt=0$. The stability curve (infinitesimally) close to $q^2=1$ is

$$2\hat{\boldsymbol{\mu}}_1^{\,2}+\hat{\boldsymbol{\mu}}_2^{\,2}=1\,. \tag{68}$$

The two curves intersect at $\hat{\boldsymbol{\mu}}_1^{\,2}=\hat{\boldsymbol{\mu}}_2^{\,2}=1/3$; in fact all of the stability boundaries intersect at this point since $\langle \mathrm{cn}^2\Phi\rangle=1-\langle \mathrm{sn}^2\Phi\rangle$ and $\langle \mathrm{dn}^2\Phi\rangle=1-q^2\langle \mathrm{sn}^2\Phi\rangle$. These two bounding stability lines are depicted in Figure 3. The stability boundaries for all other values of q are between these two lines, pivoting about their intersection point at $\hat{\boldsymbol{\mu}}_1^{\,2}=\hat{\boldsymbol{\mu}}_2^{\,2}=1/3$.

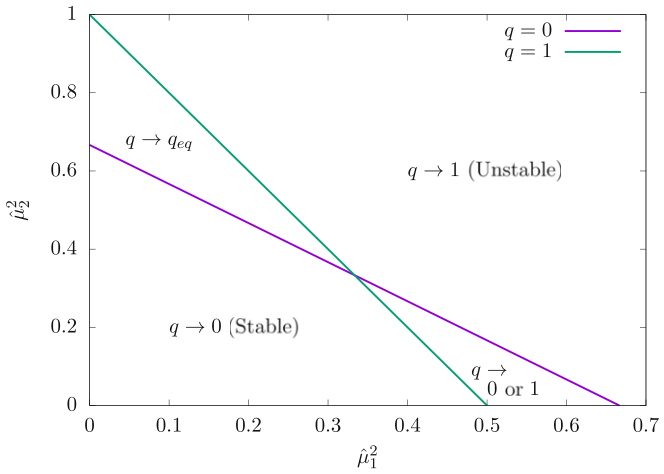

Figure 3. Stability boundaries for $q=0$ and $q=1$ and outcomes for secular evolution of q.

Figure 3 depicts the evolution outcomes for various regions in the $\mu_1^2-\mu_2^2$ phase plane. The region marked "$q\to 1$" is unconditionally unstable: if precession is excited for (μ_1^2,μ_2^2) in this region, q grows on the spindown timescale until $q=1$, where growth ceases. Conversely, the region marked "$q\to 0$" is unconditionally stable: if precession is excited for (μ_1^2,μ_2^2) in this region, q shrinks toward zero on the spindown timescale. In the two triangular regions between the $q=0$ and $q=1$ bounding curves $dq/dt=0$ at $q=q_{\rm eq}(\mu_1^2,\mu_2^2)$ for each (μ_1^2,μ_2^2). In the region marked "$q\to q_{\rm eq}$," $dq/dt<0$ for $q>q_{\rm eq}(\mu_1^2,\mu_2^2)$ and $dq/dt>0$ for $q<q_{\rm eq}(\mu_1^2,\mu_2^2)$, so if precession is excited in this region $q\to q_{\rm eq}(\mu_1^2,\mu_2^2)$ asymptotically as a result of spindown. In the region marked "$q\to 0$ or 1," $dq/dt>0$ for $q>q_{\rm eq}(\mu_1^2,\mu_2^2)$ so $q\to 1$ asymptotically if precession is excited with $q>q_{\rm eq}(\mu_1^2,\mu_2^2)$ and $dq/dt<0$ for

$q < q_{\rm eq}(\mu_1^2, \mu_2^2)$ so $q \to 0$ asymptotically if precession is excited with $q < q_{\rm eq}(\mu_1^2, \mu_2^2)$.

For precession in the $\Lambda\sqrt{1+e^2} > 1$ regime we get

$$-\frac{1}{q}\frac{dq}{dt} = \frac{ak\mu^2(L/I_3)^2}{c^3 I_3}\left\{\hat{\boldsymbol{\mu}}_3^2\left[2-\left(1+\frac{1}{q^2}\right)\langle \mathrm{sn}^2\,\Phi\rangle\right]\right.$$
$$\left.+\hat{\boldsymbol{\mu}}_2^2\left[1+\left(1-\frac{2}{q^2}\right)\langle \mathrm{sn}^2\,\Phi\rangle\right]-\left(1-\frac{\langle \mathrm{sn}^2\,\Phi\rangle}{q^2}\right)\right\}$$
$$\frac{d\psi}{dt} = \frac{ak\mu^2(L/I_3)^2\hat{\boldsymbol{\mu}}_3\hat{\boldsymbol{\mu}}_2 e}{c^3 I_3\sqrt{1+e^2}}$$
$$\times\left[\left\langle\frac{\mathrm{cn}^2\,\Phi}{\mathrm{dn}\,\Phi}\right\rangle-\left(1+\frac{1}{e^2}\right)\left\langle\frac{\mathrm{sn}^2\,\Phi}{\mathrm{dn}\,\Phi}\right\rangle\right], \quad (69)$$

where we use Equation (66) again. Equation (69) may be obtained from Equation (65) with the substitutions $\hat{\boldsymbol{\mu}}_1^2 \to \hat{\boldsymbol{\mu}}_3^2$, $e^2 \to 1/e^2$, and $q \to 1/q$. The evolution scenarios for $1/q$ analogous to those for q shown in Figure 3 may be derived using this mapping.

3. Application to FRBs

3.1. A Random Burst Model

Up to this point, we have focused on the combined effects of precession and spindown on observations of emission along a single beam in which emitted intensity is determined entirely by $\hat{\boldsymbol{b}}\cdot\hat{\boldsymbol{n}}$. For application to FRBs we develop a different model in which multiple beams pointing in random directions fire at random times with random intrinsic intensities.

To address these questions we simulate an ideal observing program consisting of daily observations over a total observing time lasting $n_{p,\rm cycle}$ precession cycles. In our idealized observing campaign, each daily observation starts 1 day after the beginning of the previous one and lasts $f_{\rm obs}$ days (2.4 hr). We assume that bursts occur at a uniform rate throughout the duration of the observing program and that $n_{\rm bursts}$ bursts occur during the total time $f_{\rm obs}n_{p,\rm cycle}P_p$ of the observations. We input P_p in days, so that the number of observing days is the integer part of P_p plus 1.

We also input the parameters of the precession model ($\epsilon_{\rm mag}$, Λ, and e^2) from which we can compute the spin frequency $\nu_\star$. We choose $\gamma(0)$ randomly in the range $[0, 2\pi]$.

The simulation starts by choosing the set $\{\Phi_j\}$ of individual burst precession phases; in the absence of spindown the corresponding burst times are $t_j = P_p\Phi_j/\Phi_{p,\rm cycle}$, and even with spindown included the burst times only differ from these times by $\mathcal{O}(\epsilon_{\rm sd})$. For each simulation there are $n_{\rm bursts}$ bursts. Ultimately, only a small fraction of these are detectable.

For each Φ_j we next determine a beam direction $\hat{\boldsymbol{b}}_j$ in the rotating frame of reference. We do this relative to a reference beam whose direction we input. In the calculations presented here we assume that this reference direction coincides with the direction of the dipole moment appearing in the spindown formula, $\hat{\boldsymbol{\mu}}$. We assume that $\hat{\boldsymbol{b}}_j$ is anywhere between two cones about $\hat{\boldsymbol{\mu}}$ defined by $\cos\theta_{\rm min} \leqslant \hat{\boldsymbol{b}}_j\cdot\hat{\boldsymbol{\mu}} \leqslant \cos\theta_{\rm max}$, adopting a uniform distribution for $\hat{\boldsymbol{b}}_j\cdot\hat{\boldsymbol{\mu}}$ over this range and a uniform direction of azimuthal angles in $[0, 2\pi]$. We could, of course, choose a different reference direction or multiple reference directions among which bursts may switch. As should already be apparent, there are many parameters in this model, and choosing a single reference direction simplifies the calculation somewhat. Our model does allow the reference direction to switch to a different one with a probability $p_{\rm flip} = 1 - f_{\rm no\ flip}$, but the results reported here are for $p_{\rm flip} = 0$.

The next step is to compute $\hat{\boldsymbol{b}}_j\cdot\hat{\boldsymbol{n}}$ for each outburst. We do this by computing $\hat{\boldsymbol{n}}(\Phi_j)$ in the rotating frame of reference from Equation (54). This requires choosing a value of the inclination angle i defined in Equation (50), which we input.

Once we have the value of $\hat{\boldsymbol{b}}_j\cdot\hat{\boldsymbol{n}}(\Phi_j) \equiv \hat{\boldsymbol{b}}_j\cdot\hat{\boldsymbol{n}}_j$ for a given outburst we can decide whether that outburst is detectable. As a first cut, we discard all bursts for which $\hat{\boldsymbol{b}}_j\cdot\hat{\boldsymbol{n}}_j < 0$ since these point away from the observer. Because we assume that each beam has an FWHM $\theta_{\rm FWHM}$ we may be discarding some bursts that could be detectable, in principle, but as long as $\theta_{\rm FWHM}$ is not too large we expect that this is not an important source of inaccuracy in our conclusions. We do not discard beams that would be eclipsed by the neutron star. To do that we would need to specify the radius r_b from which emission originates for beam b; eclipses could occur for $\cos\theta_b < 0$ and $\pi - \theta_b \lesssim R/r_b$. In most of our simulations we restrict $\cos\theta_b \geqslant 0$.

We assume a Gaussian emission pattern for each beam with an intrinsic intensity

$$I_j(\hat{\boldsymbol{b}}\cdot\hat{\boldsymbol{n}}) = I_j(1)\exp[\kappa(\hat{\boldsymbol{b}}_j\cdot\hat{\boldsymbol{n}}_j - 1)] \quad (70)$$

where, if the FWHM of the beam is $\theta_{\rm FWHM}$,

$$\kappa = \frac{\ln 2}{1-\cos(\frac{1}{2}\theta_{\rm FWHM})}; \quad (71)$$

$I_j(1)$ is the peak intensity for outburst j and

$$\int_0^1 d\mu I_j(\mu) = \frac{2\pi I_j(1)[1-\exp(-\kappa)]}{\kappa} \quad (72)$$

is the total intensity of the beam integrated over the directions. Equation (70) would be the final answer if all outbursts were equally intense intrinsically, but in general we expect a distribution of $I_j(1)$. To model this, we input a range of intrinsic intensities, and assume that the distribution of intrinsic intensities $I_j(1)$ is uniform in $\ln I_j(1)$ over the corresponding logarithmic range with a mean value of 1. (In this model we could choose a different mean value, but this would just introduce a multiplicative factor in each value of $I_j(1)$.) After selecting $\ln I_j(1)$ at random from this distribution we evaluate I_j using Equation (70).

Given $\{I_j\}$ we can find the maximum value $I_{\rm max}$. We assume that only bursts greater than $I_{\rm min} = I_{\rm max} \times (I_{\rm min}/I_{\rm max})$ are detectable, where $I_{\rm min}/I_{\rm max}$ is another input parameter. We then have the sets $\{\Phi_j\}$ and $\{I_j/I_{\rm max}\}$ for the bursts. The latter can immediately be turned into a plot of the number of detected bursts per (daily) observing session versus the precession phase, which provides a simple visual indication of whether the data reveal or conceal the precession period. The same data can be plotted as a cumulative distribution of observed burst intensities, which we shall see is different from the inputted distribution of intrinsic burst intensities.

The final step in our calculations is to determine conditions under which the spin frequency ought to be detected. We do

this by computing

$$\hat{D}(\nu_\star) = \sum_j w_j \exp[2\pi i \nu_\star t(\Phi_j)] \tag{73}$$

where $\nu_\star = \Omega(0)/2\pi$ is the (initial) spin frequency of the star and $t(\Phi_j)$ is computed from Equation (59) for selected values of $\epsilon_{\rm sd}$. In Equation (73) $\{w_j\}$ is a set of weights assigned to each detected burst. To assess the evidence for a given ν we compute $|D(\nu)|$. For totally uncorrelated t_j

$$\langle|\hat{D}(\nu_\star)|^2\rangle_{\rm uncorrelated} = \sum_j w_j^2 \tag{74}$$

so we normalize the computed values:

$$|\hat{D}(\nu_\star)|_{\rm normalized} \equiv \frac{|\hat{D}(\nu_\star)|}{\sqrt{\langle|\hat{D}(\nu_\star)|^2\rangle_{\rm uncorrelated}}}\,. \tag{75}$$

In our calculations we weight each term in Equation (73) equally, so that $w_j = 1/N_{\rm bursts}$ for $N_{\rm bursts}$ detected bursts; with this choice $\langle|D(\nu)|^2\rangle_{\rm uncorrelated} = 1/N_{\rm bursts}$, and

$$|\hat{D}(\nu_\star)|_{\rm normalized} \equiv |\hat{D}(\nu_\star)|\sqrt{N_{\rm bursts}}\,. \tag{76}$$

Another plausible choice for w_j would be $I_j/I_{\rm max}$. If the burst times are precisely periodic then $|\hat{D}(\nu_\star)| = 1$ and $|\hat{D}(\nu_\star)|_{\rm normalized} = \sqrt{N_{\rm bursts}}$. This remains true for $\nu_\star{}' = \nu_\star + \Delta\nu_\star$; the frequency shift associated with spindown, which is included in our calculation, is undetectable. For a single beam, there would be a systematic frequency shift $\mathcal{O}(\epsilon_{\rm mag})$ that depends on beam direction, but for multiple beams there is no systematic shift. The value of $|\hat{D}(\nu_\star)|$ is unaffected by shifting the burst times by a common time offset. If burst times are random, the asymptotic probability distribution of $r = |\hat{D}(\nu_\star)|\sqrt{N}$ is

$$\frac{dp(r)}{dr} = 2r\exp(-r^2) \tag{77}$$

independent of N. The mode of Equation (77) is $r = 1/\sqrt{2}$ and the mean is $\sqrt{\pi}/2$.

In our models, we evaluate $D_d(\nu_\star) = |\hat{D}(\nu_\star)|\sqrt{N_d}$ for each of the $\{d\}$ days of observations during which $\{N_d\}$ bursts are detected. According to Equation (77) the probability that $D_d > r$ is $\exp(-r^2)$ if the bursts occur randomly. If observations are done on M days the expected number of values of D_d that exceed r is $n(>r) = M\exp(-r^2)$, and the value of r for which $(n > r) = 1$ is

$$r_1(M) = \sqrt{\ln M}\,. \tag{78}$$

The probability that no values of $|\hat{D}_d(\nu_\star)|\sqrt{N_d} > r_0$ are found at random is

$$p(r_0, M) = [1 - \exp(-r_0^2)]^M$$

so for a chosen value $p = p(r_0|M)$

$$\begin{aligned} r_0(p, M) &= \frac{1}{\sqrt{\ln(1 - p^{1/M})}} = \frac{1}{\sqrt{\ln[1 - \exp(\ln p)/M]}} \\ &\approx \frac{1}{\sqrt{-\ln p/M}} = \frac{r_1(M)}{\sqrt{(-\ln p)}}\,; \end{aligned} \tag{79}$$

$r_1(M) \approx r_0(1/e,\ M)$. Below we use $r_1(M)$ to assess the detectability of $\nu_\star$ over M days by keeping track of the number of days for which $\hat{D}_d(\nu_\star)$ exceeds $r_1(M)$.

Of course the observer will not know $\nu_\star$ in advance but we presume that he/she analyzes the data for a broad range of possible spin frequencies including test values near $\nu_\star$. In our simulations, we compute $\{\hat{D}_d(\nu_\star)\}$ for each of $M = 512$ consecutive days, so $r_1(M) = \sqrt{\ln 512} = 2.498$. We focus on the day with the largest value of $\hat{D}(\nu_\star)\sqrt{N_d}$ and for that day we calculate $\hat{D}(\nu)\sqrt{N_d}$ for $N_{\rm freq}$ different frequencies. For small enough spacing between the test frequencies $\nu_\star$ ought to be very near one of the sampled frequencies; a value above $r_1(N_{\rm freq})$ is considered to be significant. In the simulations reported in Table 3 we sample frequencies spaced by $\Delta\nu/\nu = 10^{-5}$ Hz between 0.05 Hz and 5 Hz, a total of $N_{\rm freq} = 460{,}518$ frequencies, so $r_1(N_{\rm freq}) = \sqrt{\ln 460,\ 518} = 3.611$. Although we have only done frequency searches on the most promising day for each burst model, the spin frequency ought to be detectable on any day for which $\hat{D}_d(\nu_\star)\sqrt{N_d} > r_1(N_{\rm freq})$, so we tabulate the number of such days.

In Appendix B we develop an analytic theory of the probability of burst detections at a given time in our model. Equation (B.1) makes it clear that the probability depends on spin and precession frequency via $\hat{\boldsymbol{n}}(\Phi)\cdot\hat{\boldsymbol{\mu}}$. Moreover, there is no time dependence at all if the distribution of beam directions is isotropic. Thus, the observation of regular precession cycles by itself argues for a restricted range of beam directions.

3.2. Results

Given the large number of parameters, we have not done a systematic, complete exploration of the multidimensional phase space of models. However, we have explored numerous particular cases to look for trends related to the two phenomenological questions above. In doing this, we have held one parameter not listed in Table 3 fixed for most runs: the initial value of the random number seed. Normally, this is Monte Carlo malpractice. Two models with identical initial random number seeds, the same value of $n_{\rm bursts}$, and the same ranges of $\cos\theta_b$ and $I_j(1)$ will start with identical sets of outbursts; that is, $\{\Phi_j, \hat{\boldsymbol{b}}_j, I_j(1)\}$ will be the same. However, two models with the same e^2 but different values of Λ will have different $\{\hat{\boldsymbol{n}}_j\}$ and hence different $\{\hat{\boldsymbol{b}}_j\cdot\hat{\boldsymbol{n}}_j\}$ and different intensities $\{I_j\}$ so their subsets of detectable outbursts will be different. Models with different ranges of $\cos\theta_b$ and $I_j(1)$ start with identical sets of $\{\Phi_j\}$, which isolates the differences in properties of detectable bursts associated with emitting geometry and precession. Here and there we have verified that the initial random number seed is not critical to qualitative features of the results.

For $n_{\rm bursts}$ in a total observing time $t_{\rm obs} = f_d n_{p,{\rm cycle}} P_p$, the burst rate is $n_{\rm bursts}/t_{\rm obs}$; for the simulations listed in Table 3 $t_{\rm obs} = 51.2$ days and the burst rate is $1{,}024{,}000/51.2\ {\rm days} = 20{,}000\ {\rm days}^{-1} = 0.231$ Hz. For our simulations, $\nu_\star \simeq 0.1$, 0.15, 1, or 1.5 Hz so the number of outbursts per spin period ranges from $\simeq$0.15 to $\simeq$2.3. If all of these bursts were detectable, the spin frequency of the magnetar would be easy to find. In the simulation results, the burst detection efficiency is *at most* $\simeq$4%, which would correspond to *at most* of the order of one burst per 10 spin periods, which, although not large, should still suffice to uncover the underlying spin period. The total number of outbursts is chosen so that the average number

Table 3
Simulated Burst Models[a]

P_p (days)	$\epsilon_{\rm mag}$	Λ	$\nu_\star$ (Hz)	$\cos\theta_b$[b]	$D_{\rm max}$ (day)[c]	$N_{\rm bursts}$ (%)[d]	$N_d(512)$[e]	$N_d(N_{\rm freq})$[f]	Description
160	10^{-6}	0.2	0.1521	[0.99, 1]	13.6 (411)	37,596 (3.7%)	399	384	pulsar-like
160	10^{-7}	0.2	1.521	[0.99, 1]	13.0 (414)	37,017 (3.6%)	403	386	pulsar-like
16.4	10^{-5}	0.2	0.1484	[0.99, 1]	13.0 (48)	40,280 (3.9%)	417	403	pulsar-like
16.4	10^{-6}	0.2	1.484	[0.99, 1]	12.8 (109)	39,497 (3.9%)	416	403	pulsar-like
160	10^{-6}	0.2	0.1521	[0, 1]	4.46 (443)	29,864 (2.9%)	114	13	hemisphere
160	10^{-7}	0.2	1.521	[0, 1]	4.40 (427)	29,663 (2.9%)	114	11	hemisphere
16.4	10^{-5}	0.2	0.1484	[0, 1]	4.24 (341)	29,333 (2.9%)	110	8	hemisphere
16.4	10^{-6}	0.2	1.484	[0, 1]	4.05 (488)	29,456 (2.9%)	109	12	hemisphere
160	10^{-6}	0.2	0.1521	[0.1, 0.8]	3.22 (438)	28,965 (2.8%)	17	0	inter-cone
160	10^{-7}	0.2	1.521	[0.1, 0.8]	3.79 (377)	29,030 (2.8%)	24	2	inter-cone
16.4	10^{-5}	0.2	0.1484	[0.1, 0.8]	2.90 (37)	28,630 (2.8%)	8	0	inter-cone
16.4	10^{-6}	0.2	1.484	[0.1, 0.8]	3.36 (168)	28,290 (2.8%)	13	0	inter-cone
160	10^{-6}	0.44	0.1071	[0.99, 1]	13.1 (352)	16,682 (1.6%)	181	164	pulsar-like
160	10^{-7}	0.44	1.071	[0.99, 1]	12.6 (32)	16,541 (1.6%)	182	169	pulsar-like
16.4	10^{-5}	0.44	0.1045	[0.99, 1]	12.9 (86)	16,747 (1.6%)	181	168	pulsar-like
16.4	10^{-6}	0.44	1.045	[0.99, 1]	12.9 (431)	16,784 (1.6%)	179	166	pulsar-like
160	10^{-6}	0.44	0.1071	[0, 1]	5.07 (50)	21,334 (2.1%)	326	157	hemisphere
160	10^{-7}	0.44	1.071	[0, 1]	4.85 (445)	21,158 (2.1%)	317	143	hemisphere
16.4	10^{-5}	0.44	0.1045	[0, 1]	4.80 (418)	20,322 (2.0%)	336	149	hemisphere
16.4	10^{-6}	0.44	1.045	[0, 1]	5.20 (187)	20,799 (2.0%)	343	177	hemisphere
160	10^{-6}	0.44	0.1071	[0.1, 0.8]	5.61 (390)	22,160 (2.2%)	271	179	inter-cone
160	10^{-7}	0.44	1.071	[0.1, 0.8]	5.65 (433)	22,335 (2.2%)	278	177	inter-cone
16.4	10^{-5}	0.44	0.1045	[0.1, 0.8]	5.46 (46)	21,615 (2.1%)	299	185	inter-cone
16.4	10^{-6}	0.44	1.045	[0.1, 0.8]	5.37 (385)	21,268 (2.1%)	300	193	inter-cone

Notes.
[a] Consecutive daily observations lasting 0.1 days each for 512 days, observer at $i = 52°$. A total of 1,024,000 outbursts. Beamwidth $\theta_{\rm FWHM} = 20°$. Intrinsic intensity range a factor of 1000; ratio of minimum to maximum observed intensities $I_{\rm min}/I_{\rm max} = 0.01$. $\epsilon_{\rm sd} = 0$.
[b] Range of beam offsets axisymmetric relative to symmetry axis at $\hat{\boldsymbol{e}}_3\cos\theta_\mu + \sin\theta_\mu(\hat{\boldsymbol{e}}_1\cos\varphi_\mu + \hat{\boldsymbol{e}}_2\sin\varphi_\mu)$ with $(\theta_\mu, \varphi_\mu) = (30°, 40°)$.
[c] Maximum value of $\hat{D}_d\sqrt{N_d}$ and day on which it occurs.
[d] Total number of detectable bursts and fraction of total number of outbursts.
[e] Number of days for which $\hat{D}_d\sqrt{N_d}$ exceeds $\sqrt{\ln 512} = 2.498\ldots$.
[f] Number of days for which $\hat{D}_d\sqrt{N_d}$ exceeds $\sqrt{\ln N_{\rm freq}} = 3.611\ldots$.

of *detected* bursts per day would turn out to be ∼50 in the simulations. This detection rate is comparable to the rate reported by Li et al. (2021) for about 50 days of observations of FRB 121102. No convincing evidence for a spin frequency was found by Li et al. (2021).

Table 3 tabulates the results for 16 simulations. For all of these

1. $e^2 = 10$,
2. the distribution of intrinsic intensities ranges over a factor of 1000,
3. the beamwidth is $\theta_{\rm FWHM} = 20°$,
4. bursts are detectable over a range of observed intensities $I_{\rm max}/I_{\rm min} = 1000$,
5. the distribution of beam directions is axisymmetric about the symmetry axis $\hat{\boldsymbol{\mu}} = \hat{\boldsymbol{e}}_3\cos\theta\mu + \sin\theta_\mu(\hat{\boldsymbol{e}}_1\cos\varphi_\mu + \hat{\boldsymbol{e}}_2\sin\varphi_\mu)$ with $(\theta_\mu, \varphi_\mu) = (30°, 40°)$,
6. there are daily observations lasting 0.1 days each over a total time span of 512 days, and
7. the observer is at $i = 52°$ relative to the spin angular momentum of the star (Equation (50)).

The average number of bursts per day is ∼30–60 for all of the tabulated models. Although the tabulated models are for $\epsilon_{\rm sd} = 0$ we do not regard this as an essential limitation for two reasons. First, as omniscient simulators, we can nullify the effects of spindown entirely by adjusting the value of the frequency tested from $\nu_\star$ to $\nu_{\star,d}$; our code allows us to do this, and we have verified that $\hat{D}_d(\nu_{\star,d})$ with $\epsilon_{\rm sd} \neq 0$ is virtually the same as $\hat{D}(\nu_\star)$ with $\epsilon_{\rm sd} = 0$. Second, we do frequency searches on the most promising day with $\epsilon_{\rm sd} \neq 0$ and detect frequency shifts for large enough spindown compared to our frequency resolution.

The table is divided into two categories, $\Lambda = 0.2$ and $\Lambda = 0.44$; more precisely $q^2 = 5/12$ for the upper half of the table and $q^2 = 12/5$ for the lower half. Each half is subdivided into three parts that are distinguished by different ranges of beam directions:

1. "pulsar-like" models only allow beams in a very narrow cone of angles around $\hat{\boldsymbol{\mu}}$, $0.99 \leqslant \cos\theta_b \leqslant 1$;
2. "hemisphere" models allow beams in any direction in the outward hemisphere relative to $\hat{\boldsymbol{\mu}}$, $0 \leqslant \cos\theta_b \leqslant 1$; and
3. "inter-cone" models allow beams between the cones defined by $\cos\theta_{\rm min} = 0.1$ and $\cos\theta_{\rm max} = 0.8$ around $\hat{\boldsymbol{\mu}}$.

Inter-cone models exclude beams in a fairly narrow cone near the symmetry axis as well as beams orthogonal to it. A number of trends are apparent in Table 3:

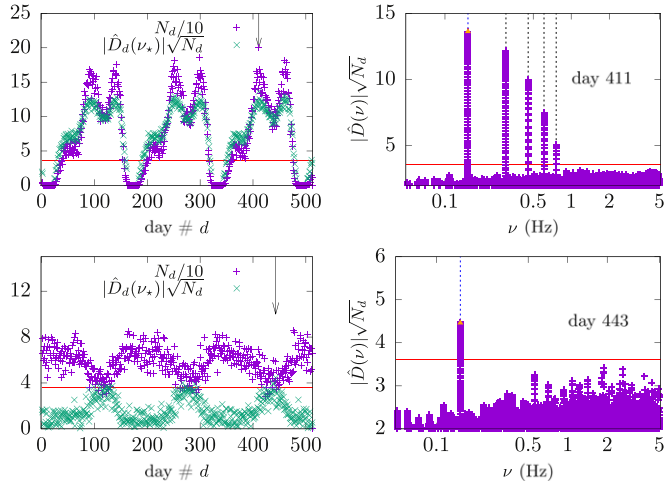

Figure 4. Results for the most promising days for spin frequency detection for two models with $P_p = 160$ days, $\Lambda = 0.2$, and $\epsilon_{\rm mag} = 10^{-6}$. A pulsar-like model is shown in the top row and a hemisphere model in the bottom row. See Table 3 for details. The left panels show the number of bursts per day, N_d, divided by 10 (purple crosses) and the value of $|\hat{D}_d(\nu_\star)|\sqrt{N_d}$ on each day (green crosses). Downward-pointing arrows indicate the days with the largest value of $|\hat{D}_d(\nu_\star)|\sqrt{N_d}$, days 411 (top/pulsar-like) and 443 (bottom/hemisphere). The right panels show the results of computing $|\hat{D}_d(\nu)|\sqrt{N_d}$ on these days for frequencies 0.05 Hz $\leqslant \nu \leqslant$ 5 Hz with equal logarithmic spacing $\Delta\nu/\nu \simeq 10^{-5}$. The horizontal red lines are at $|\hat{D}_d(\nu)|\sqrt{N_d} = \sqrt{\ln N_{\rm freq}} \simeq 3.611$, the value above which about one point ought to appear at random according to the Rayleigh distribution. For the models shown, detecting the spin frequency ought to be relatively easy: the fundamental and four harmonics show up significantly for the pulsar-like model but just the fundamental shows up for the hemisphere model.

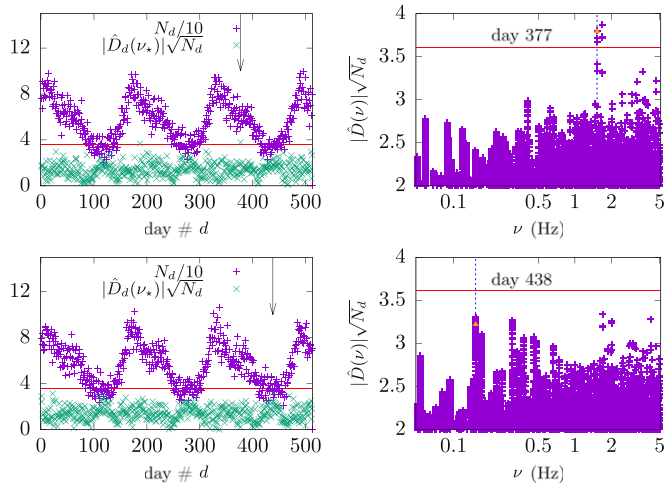

Figure 5. Results for the most promising days for spin frequency detection for two inter-cone models with $P_p = 160$ days, $\Lambda = 0.2$, and $\epsilon_{\rm mag} = 10^{-7}$ (top) and $\epsilon_{\rm mag} = 10^{-6}$ (bottom). The format is the same as that in Figure 4. For these models the spin frequency is not detectable unambiguously on their respective most promising days.

1. more bursts are detectable for $\Lambda = 0.2$ than for $\Lambda = 0.44$ in all cases;
2. for either value of Λ all subcategories—pulsar-like, hemisphere, and inter-cone—give similar results irrespective of the value of $\epsilon_{\rm mag}$;
3. $\nu_\star$ is readily detectable on $\sim$30% of days for $\Lambda = 0.44$ for pulsar-like, hemisphere, and inter-cone geometries;
4. $\nu_\star$ is detectable on $\lesssim$3% of all days for hemisphere models with $\Lambda = 0.2$, but reproducible results for $\nu_\star$ (modulo spindown) ought to emerge in a dedicated program of nearly daily observations that last long enough; and
5. $\nu_\star$ is largely undetectable for inter-cone models with $\Lambda = 0.2$.

The uniformity of results within the various subcategories is not a complete surprise since 160/16.4 is near 10 so models with $P_p = 160$ days and a given value of $\epsilon_{\rm mag}$ ought to resemble models with $P_p = 16.4$ days and $10\epsilon_{\rm mag}$ closely. The dependence on $\epsilon_{\rm mag}$ for a given value of P_p is weak. The detection criteria in our simulations only depend on spin frequency implicitly via $\hat{\boldsymbol{b}}\cdot\hat{\boldsymbol{n}}(\Phi)$, but this dependence is weak because $\hat{\boldsymbol{b}}$ varies widely and stochastically (except in the pulsar-like models). We expect that as long as the time between bursts is long compared with $1/\nu_\star$ final results should be insensitive to $\epsilon_{\rm mag}$.

Although we have not tabulated results for models in which beams can point in any direction (i.e., $-1 \leqslant \cos\theta_b \leqslant 1$) we have simulated such models; in general neither $\nu_\star$ nor P_p is apparent in the results.

Figure 4 shows the numerical results for two models where $\nu_\star$ ought to be detected. All of these results are for $P_p = 160$ days, $\epsilon_{\rm mag} = 10^{-6}$, and $\Lambda = 0.2$, so that $\nu_\star = 0.1521$ Hz. The top panels are for the pulsar-like case and the bottom are for the hemisphere case. The left panels in both rows show $N_d/10$ for each day (purple crosses); the precession cycle is evident in both panels. These panels also show $\hat{D}_d(\nu_\star)\sqrt{N_d}$ for each day (green crosses), with the day on which $\hat{D}_d(\nu_\star)\sqrt{N_d}$ is largest indicated by a downward arrow. The horizontal red line in each figure is at $r_1(N_{\rm freq}) = \sqrt{\ln N_{\rm freq}} \simeq 3.611$, which we take to be the threshold for detection of $\nu_\star$. The right panels show the results of a period search on the most favorable day for detecting $\nu_\star$ using $N_{\rm freq} = 460{,}518$ test frequencies spaced at equal logarithmic intervals $\Delta\nu/\nu \simeq 10^{-5}$ between 0.05 Hz and 5 Hz. The value of $\hat{D}_d(\nu_\star)\sqrt{N_d}$ exactly at $\nu_\star$ is also shown as an orange triangle. The leftmost vertical dashed lines are at the spin frequencies for these two models; for the pulsar-like model vertical dashed lines at four harmonics of $\nu_\star$ are also shown. The spin frequency and four harmonics are found easily for the pulsar-like model; the spin frequency is also found for the hemisphere model.

Figure 5 shows the numerical results for two inter-cone models with $P_p = 160$ days and $\epsilon_{\rm mag} = 10^{-7}$ (top) and $\epsilon_{\rm mag} = 10^{-6}$ (bottom). For $\epsilon_{\rm mag} = 10^{-7}$ the spin frequency should be detectable, whereas for $\epsilon_{\rm mag} = 10^{-6}$ it is not. The spin frequency would be found significantly for $\epsilon_{\rm mag} = 10^{-7}$, but a slightly larger value of $|\hat{D}(\nu)|\sqrt{N_d}$ is found around 1.7 Hz. This is not particularly troubling since both frequencies have values of $|\hat{D}(\nu)|\sqrt{N_d}$ close to $r_1(N_{\rm freq})$, but it suggests that $\nu_\star$ would not be detected on this particular day. (We reran this case with a different random number seed and found that $|\hat{D}(\nu)|\sqrt{N_d} < r_1(N_{\rm freq})$ on all days.) The spin frequency would not be found for $\epsilon_{\rm mag} = 10^{-6}$.

So far, we have concentrated on searching for $\nu_\star$ on individual days, presenting frequency spectra only on the most promising days for detection. Alternatively, the frequency search can be performed on the entire data set. Figure 6 shows the results for the cumulative value $|\hat{D}(\nu_\star, \leqslant d)|$ computed by performing the sum in Equation (73) over the $N(\leqslant d)$ bursts detected up to the end of day d and multiplying by $\sqrt{N(\leqslant d)}$.

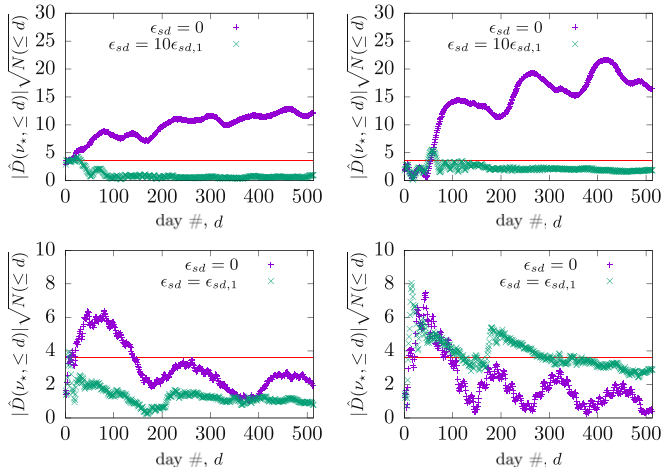

Figure 6. Cumulative $|\hat{D}(\nu_\star, \leqslant d)|\sqrt{N(\leqslant d)}$ as a function of day number d. Top: $P_p = 160$ days, $\epsilon_{\rm mag} = 10^{-6}$ nested-cone models with $\Lambda = 0.2$ (left) and $\Lambda = 0.44$ (right), and $\epsilon_{\rm sd} = 0$ (purple crosses) and $\epsilon_{\rm sd} = 10\epsilon_{\rm sd,1}$ (green crosses). Bottom: $P_p = 16.4$ days, $\epsilon_{\rm mag} = 10^{-5}$ with $\Lambda = 0.2$ (left) and $\Lambda = 0.44$ (right), and $\epsilon_{\rm sd} = 0$ (purple crosses) and $\epsilon_{\rm sd} = \epsilon_{\rm sd,1}$ (green crosses).

All four panels in Figure 6 are computed for a nested-cone geometry with $0.1 \leqslant \cos\theta_b \leqslant 0.8$. The top panels are for $P_p = 160$ days and $\epsilon_{\rm mag} = 10^{-6}$ and the bottom for $P_p = 16.4$ days and $\epsilon_{\rm mag} = 10^{-5}$ so spin frequencies are comparable in all cases. The left panels are for $\Lambda = 0.2$, where Table 3 indicates no promising days for burst detections, and the right panels are for $\Lambda = 0.44$, for which we expect ≈200 promising days. The top left panel shows that the value of $|\hat{D}(\nu_\star, \leqslant d)|\sqrt{N(\leqslant d)}$ generally increases with d for $\epsilon_{\rm sd} = 0$, apart from fluctuations, suggesting that detection may be possible in a cumulative analysis. However, Equation (64) implies that $\epsilon_{\rm sd}/\epsilon_{\rm sd,1} \approx 17 B_{D,14}^2$ for the top left panel in Figure 6 and $\approx 6 B_{D,14}^2$ for the right panel. At these levels, the accumulated spindown over many days of observation becomes important, and discovering $\nu_\star$ from a cumulative analysis that neglects spindown is problematic. The situation for $P_p = 16.4$ days appears to be more complicated. As the left panel shows, although $|\hat{D}(\nu_\star, \leqslant d)|\sqrt{N(\leqslant d)}$ increases at first for $\epsilon_{\rm sd} = 0$, ultimately it decreases while fluctuating considerably; the same sort of behavior is evident in the right panel. For these cases, $\epsilon_{\rm sd} \approx 0.17 B_{D,14}^2\, \epsilon_{\rm sd,1}$ and $0.06 B_{D,14}^2\, \epsilon_{\rm sd,1}$, respectively, so spindown is less important for $B_{D,14} = 1$. We show what happens for $\epsilon_{\rm sd} = \epsilon_{\rm sd,1}$ in both panels: spindown this fast further suppresses accumulation of evidence for $\nu_\star$ in the left panel, but actually can enhance it, at least for a while, in the case depicted in the right panel.

4. Conclusions

The first part of this paper has been devoted to the theory of precession of neutron stars whose distortions are due to strong internal magnetic fields. We have stressed that unless internal field strengths are very large precession ought to be frustrated by the pinning of neutron superfluid vortices, to nuclei in the crust (Shaham 1977) and to flux tubes associated with type II proton superconductivity in the core (Link 2003). We argue that internal magnetic fields with strength $\gtrsim 10^{16}$ G must pervade the star if precession is to be possible. As we have discussed, fields this strong can prevent proton superconductivity in the core (see Equation (1) and the associated discussion), are strong enough to shatter the crust, and may even prevent or at least substantially alter neutron superfluidity in both core and crust (see Equation (3) and the associated discussion). Avoiding vortex line pinning is a very stringent requirement: even very localized regions where neutron vortices pin can prevent slow precession if they comprise just a modest fraction—say 0.1%—of the moment of inertia of the star (Shaham 1977).

These considerations have led us to examine the implications of a three-component model of the magnetic field in magnetars: (1) a dipole component with characteristic strength $\sim 10^{14}$ G; (2) a toroidal component with characteristic strength $\sim 10^{15}$–10^{16} G; and (3) a disordered field with characteristic strength $\sim 10^{16}$ G. Because the volume occupied by the toroidal field may be limited (as in the models of Akgün et al. 2013) the disordered component may be critical for suppressing superfluidity and superconductivity, which is a necessary condition for slow precession. Since small-scale, disordered fields may decay in a timescale ∼1000 yr (see Equation (30); Reisenegger & Goldreich 1992; Glampedakis et al. 2011; Passamonti et al. 2017; Gusakov et al. 2017) a magnetar may only precess for a relatively short time, until the disordered field that enables slow precession decays significantly. The decay of the disordered field may also end the bursting phase in the life of a magnetar, for this component contains most of the stellar magnetic energy and is capable of stimulating internal fluctuations that propagate into the magnetosphere, where they might trigger burst activity.

The illustrative but schematic models for magnetic distortion in Section 2.2 imply that the resulting quadrupolar deformation is almost certainly triaxial and probably prolate. We developed the theory of triaxial precession in Section 2.3, noting in particular that large-amplitude precession can be excited as a result of small shearing motions involving only tiny fractions of the magnetic energy of the star. We included spindown in the theory developed in that section (using the spindown formula found by Li et al. 2012): Section 2.4 developed a timing model $t(\Phi)$ that relates clock time to precession phase when spindown is included, and Section 2.5 developed the secular effects of spindown on precession dynamics for the triaxial case, a generalization of Goldreich (1970) that dealt with axisymmetric, oblate precession. We have yet to explore possible phenomenological implications of the secular evolution. The timing model exhibits the expected systematic spindown, as altered by precession, but also includes important cyclical terms that vary periodically with precession (discussed less generally by Cordes 1993).

In the introduction, we asked whether the spin frequency ought to be detected for a magnetar precessing with a known precession period. So far, no spin frequency is apparent in either FRB 121102 or FRB 180916.J0158+65. This may be simply because we have not detected enough bursts from these FRBs to find evidence for their spin periods, or it may be that doing so is virtually impossible because of the physical properties of these objects and the FRB mechanism. If the reason we have yet to detect spin frequencies is that we need more burst detections, how sensitive and systematic must an observing program be to find the spin convincingly?

In order to address this issue we constructed a specific stochastic model for FRBs in Section 3. In this model, FRBs are associated with outbursts that occur randomly in time with energy output that is beamed into a range of directions that we select. Generally, we confine the beam directions to be outward

relative to a reference (magnetic) axis; for beam directions that are totally random neither the spin frequency nor the precession period is discernible. Thus, the existence of repeated precession cycles for FRB 121102 and FRB 180916.J0158+65 already shows that they are not caused by beamed emission directed entirely at random.

Our model offers some hope for detecting spin frequencies, as precession implies that there is a bias that favors detection of optimally directed beams. The analytic model in Appendix B demonstrates that the dependence on both the spin and precession frequencies arises from the motion of the unit vector to the observer in the rotating frame of reference, but the dependences may be very weak. In order to assess whether the spin frequency can be detected, we computed $r_d(\nu_\star) = |\hat{D}_d(\nu_\star)|\sqrt{N_d}$ for each day d in our hypothetical observing program; N_d is the number of bursts detected on day d and $\hat{D}(\nu)$ is defined in Equation (73). For a frequency search with $N_{\rm freq} = 460{,}518$ frequencies spanning the range 0.05–5 Hz with equal logarithmic spacing, $\Delta\nu/\nu = 10^{-5}$, on any given day, the largest value that should arise at random is approximately $r_1(N_{\rm freq}) = \sqrt{\ln N_{\rm freq}} \approx 3.611$. The spin frequency ought to be detectable on days when $r_d(\nu_\star) > r_1(N_{\rm freq})$. Finding $\nu_\star$ is likelier for cases where the number of days with $r_d(\nu_\star) > r_1(N_{\rm freq})$ is a substantial fraction of the total number of days on which observations are done.

Although we have only computed a modest number of models, the results reported in Table 3 divide qualitatively into two classes depending on the value of $q^2 = e^2\Lambda^2/(1-\Lambda^2)$. Based on the criterion described above, we believe that detecting the burst frequency is likely when $q^2 > 1$ irrespective of the value of $\epsilon_{\rm mag}$ or the distribution of beam directions. However, the situation for $q^2 < 1$ is more complicated. Although detecting $\nu_\star$ ought to be easy for pulsar-like models, where the range of beam directions relative to the reference axis is small, widening this range diminishes the odds of detection considerably. Allowing beam directions anywhere in the outward hemisphere relative to the axis would lead to detections on $\lesssim$3% of the days during which observations are done. But restricting beams to avoid directions moderately close to the axis and perpendicular to it makes detecting the spin frequency nearly impossible in our models.

Finally, the simulations all indicate that the fraction of outbursts that are ultimately detectable is small: the largest fraction of all outbursts that are detectable in our models is 3.9%, for pulsar-like models with $q^2 < 1$, and is at most 2.9% for all other models we have simulated. That means that the model simulated here is not very energy-efficient, in that at least ∼25–50 times as much energy is being emitted in FRBs as we would deduce from observations. One might expect that beaming mitigates the energetic requirements, and of course for a given peak intensity the total emitted intensity is $\propto 1/\kappa \sim \theta^2_{\rm FWHM}$. Our calculations only cover a single Gaussian beamwidth, $\theta_{\rm FWHM} = 20°$. Lowering $\theta_{\rm FWHM}$ reduces the total number of detections at a fixed outburst rate, which we have found to be roughly $\propto\theta^2_{\rm FWHM}$ via sporadic exploration of the phase space. Assuming this to be true, the overall amount of energy required in the stochastic model would be roughly independent of $\theta_{\rm FWHM}$ for small values of the beamwidth: the total emission per beam is $\propto\theta^2_{\rm FWHM}$ but the number of undetected beams per detected beam is $\propto 1/\theta^2_{\rm FWHM}$. Moreover, with fewer burst detections per day uncovering the magnetar spin frequency becomes harder.

S.C. and J.M.C. acknowledge support from the National Science Foundation (NSF) under AAG award 1815242 and are members of the NANOGrav Physics Frontiers Center supported by NSF award 1430284. We thank the referee for a review that identified parts of the original manuscript that needed additional clarification. I.W. thanks Jeevak Parpia, Armen Sedrakian, and Peter Rau for helpful comments.

Appendix A
Useful Integrals and Details of Computation of the Timing Model

Using Table 4 we find

$$\begin{aligned}
&\int_0^\Phi d\Phi' \int_0^{\Phi'} d\Phi''\, {\rm cn}\,\Phi''\,{\rm sn}\,\Phi'' \\
&= \frac{1}{Q^2}\int_0^\Phi d\Phi'(1 - {\rm dn}\,\Phi') = \frac{\Phi - \varphi(\Phi)}{Q^2} \\
&= \frac{\Phi(1 - \langle {\rm dn}\,\phi\rangle)}{Q^2} + \frac{\Phi\langle {\rm dn}\,\Phi\rangle - \varphi(\Phi)}{Q^2} \\
&\equiv \frac{\Phi(1 - \langle {\rm dn}\,\phi\rangle)}{Q^2} + C_2(\Phi|Q) \\
&\int_0^\Phi d\Phi' \int_0^{\Phi'} d\Phi''\, {\rm cn}\,\Phi''\,{\rm dn}\,\Phi'' = \int_0^\Phi d\Phi'\,{\rm sn}\,\Phi' \\
&= \frac{1}{Q}\ln\left[\frac{{\rm dn}(\Phi) - Q\,{\rm cn}(\Phi)}{1-Q}\right] \equiv C_3(\Phi|Q) \\
&\int_0^\Phi d\Phi' \int_0^{\Phi'} d\Phi'\,{\rm sn}\,\Phi''\,{\rm dn}\,\Phi'' = \int_0^\Phi d\Phi'(1 - {\rm cn}\,\Phi') \\
&= \Phi - \frac{\sin^{-1}[Q\sin\varphi(\Phi)]}{Q} \equiv \Phi - C_4(\Phi|Q)
\end{aligned} \tag{A.1}$$

where we rewrite the first integral to isolate the secular term from the strictly periodic one. The third integral also has a secular term. These terms are $\propto\Phi\propto\phi$ and, in effect, renormalize the initial spin period.

Finally, we consider terms $\propto {\rm sn}^2\,\Phi$; we clearly need to remove $\langle {\rm sn}^2\,\Phi\rangle$, which produces a term in $t(\phi)$ that is $\propto\phi^2$. We assume that what remains is periodic, so we focus just on the period starting at $\Phi = 0$. We then find

$$\begin{aligned}
C_1(\Phi|Q) &\equiv \int_0^\Phi d\Phi' \int_0^{\Phi'} d\Phi''(\,{\rm sn}^2\,\Phi'' - \langle\,{\rm sn}^2\,\Phi\rangle) \\
&= \int_0^\Phi \frac{d\Phi'[F(\varphi(\Phi')\,|\,Q) - E(\varphi(\Phi')\,|\,Q)]}{Q^2} - \frac{\langle\,{\rm sn}^2\,\Phi\rangle\Phi^2}{2} \\
&= \frac{\Phi^2}{2}\left(\frac{1}{Q^2} - \langle\,{\rm sn}^2\,\Phi\rangle\right) - \frac{1}{Q^2}\int_0^\Phi d\phi' E(\varphi(\Phi') \\
&= \frac{\Phi^2 E(\pi/2\,|\,Q)}{2Q^2F(\pi/2\,|\,Q)} - \frac{1}{Q^2}\int_0^\Phi d\Phi' E(\varphi(\Phi')|Q)\,.
\end{aligned} \tag{A.2}$$

Available routines for evaluating complete elliptic functions return values for $\varphi(\Phi) \leqslant \pi/2$ (Press et al. 2002), which covers all of the values of these functions; for $\pi/2 < \varphi \leqslant \pi$ we substitute

$$\begin{aligned}
E(\varphi|Q) &= E(\pi|Q) - E(\pi - \varphi|Q) \\
&= 2E(\pi/2|Q) - E(\pi - \varphi|Q)
\end{aligned} \tag{A.3}$$

Table 4
Useful Integrals and Averages

Integral[a]	Result
$\int_0^\Phi d\Phi'\,\mathrm{dn}(\Phi')$	$\varphi(\Phi)$
$\int_0^\Phi d\Phi'\,\mathrm{cn}\,\Phi'\,\mathrm{dn}\,\Phi'$	$\mathrm{sn}\,\Phi$
$\int_0^\Phi d\Phi'\,\mathrm{sn}\,\Phi'\,\mathrm{dn}\,\Phi'$	$-\,\mathrm{cn}\,\Phi$
$\int_0^\Phi d\Phi'\,\mathrm{cn}\,\Phi' = \int_0^{\varphi(\Phi)} \frac{d\varphi\cos\varphi}{\sqrt{1-Q^2\sin^2\varphi}}$	$\frac{\sin^{-1}[Q\sin\varphi(\Phi)]}{Q}$[b]
$\int_0^\Phi d\Phi'\,\mathrm{sn}\,\Phi' = \int_0^{\varphi(\Phi)} \frac{d\varphi\sin\varphi}{\sqrt{1-Q^2+Q^2\cos^2\varphi}}$	$\frac{1}{Q}\ln\left[\frac{1+Q}{Q\,\mathrm{cn}\,\Phi+\sqrt{Q^2\,\mathrm{cn}^2\,\Phi+1-Q^2}}\right] = \frac{1}{Q}\ln\left[\frac{\mathrm{dn}(\Phi)-Q\,\mathrm{cn}(\Phi)}{1-Q}\right]$
$\int_0^\Phi d\Phi'\,\mathrm{sn}^2\,\Phi'$	$\frac{1}{Q^2}[F(\varphi(\Phi)\vert Q) - E(\varphi(\Phi)\vert Q)]$
	$E(\varphi\vert Q) = \int_0^\varphi d\varphi'\sqrt{1-Q^2\sin^2\varphi'}$
$\int_0^\Phi d\Phi'\,\mathrm{sn}\,\Phi'\,\mathrm{cn}\,\Phi'$	$-\frac{\mathrm{dn}\,\Phi}{Q^2}$
$\langle\,\mathrm{sn}^2\,\Phi\,\rangle$	$\frac{1}{Q^2}\left[1-\frac{E(\pi/2\,\vert\,Q)}{F(\pi/2\,\vert\,Q)}\right]$
$\langle\,\mathrm{dn}\,\Phi\,\rangle$	$\frac{\pi/2}{F(\pi/2\,\vert\,Q)}$
$\left\langle\frac{1}{\mathrm{dn}\,\Phi}\right\rangle$	$\frac{\pi/2}{F(\pi/2\,\vert\,Q)\sqrt{1-Q^2}}$
$\left\langle\frac{\mathrm{sn}^2\,\Phi}{\mathrm{dn}\,\Phi}\right\rangle$	$\frac{\pi/2}{Q^2F(\pi/2\,\vert\,Q)}\left(\frac{1}{\sqrt{1-Q^2}}-1\right)$
$\left\langle\frac{\mathrm{cn}^2\,\Phi}{\mathrm{dn}\,\Phi}\right\rangle$	$\frac{\pi/2}{Q^2F(\pi/2\,\vert\,Q)}(1-\sqrt{1-Q^2})$

Notes.
[a] $Q = q$ for $q < 1$ and $Q = 1/q$ for $q > 1$.
[b] $-\pi/2 \leqslant \sin^{-1}z \leqslant \pi/2$.

to get

$$\int_0^\Phi d\Phi' E(\Phi'|Q) = \int_0^{\pi/2} \frac{d\varphi E(\varphi|Q)}{\sqrt{1-q^2\sin^2\varphi}}$$
$$+ 2E(\pi/2|Q)(\Phi - F(\pi/2|Q)) - \int_{\pi/2}^{\varphi(\Phi)} \frac{d\varphi' E(\pi-\varphi'|Q)}{\sqrt{1-Q^2\sin^2\varphi'}}$$
$$= \int_0^{\pi/2} \frac{d\varphi E(\varphi|Q)}{\sqrt{1-q^2\sin^2\varphi}} + 2E(\pi/2|Q)(\Phi - F(\pi/2|Q))$$
$$- \int_{\pi-\varphi(\Phi)}^{\pi/2} \frac{d\psi E(\psi|Q)}{\sqrt{1-Q^2\sin^2\psi}}$$
$$= 2E(\pi/2|Q)(\Phi - F(\pi/2|Q))$$
$$+ \int_0^{\pi-\varphi(\Phi)} \frac{d\psi E(\psi|Q)}{\sqrt{1-Q^2\sin^2\psi}}. \qquad \text{(A.4)}$$

$C_1(\Phi|Q) = 0$ at $\Phi = 0$ and $\Phi = 2F(\pi/2|Q)$, and has its peak value at $\Phi = F(\pi/2|Q)$.

Figure 7 shows the results for $C_i(\Phi|Q)$ for one precession cycle for $Q = 0.3$, 0.6, and 0.9, and also for $Q = 0$ (thin black line), for which the limiting forms are

$$C_1(\Phi) = \frac{\cos 2\Phi - 1}{8} \quad C_2(\Phi) = -\frac{\sin 2\Phi}{8}$$
$$C_3(\Phi) = 1 - \cos\Phi \quad C_4(\Phi) = \sin\Phi\,. \qquad \text{(A.5)}$$

The functions $C_1(\Phi|q)$ and $C_2(\Phi|q)$ have periods equal to half of the precession period. The functions $C_3(\Phi|q)$ and $C_4(\Phi|q)$ have periods equal to a full precession cycle. Notice that although there is no secular variation of $C_3(\Phi|q)$ this function has a nonzero mean over its full cycle of variation, which would manifest itself as an offset in $t(\phi)$.

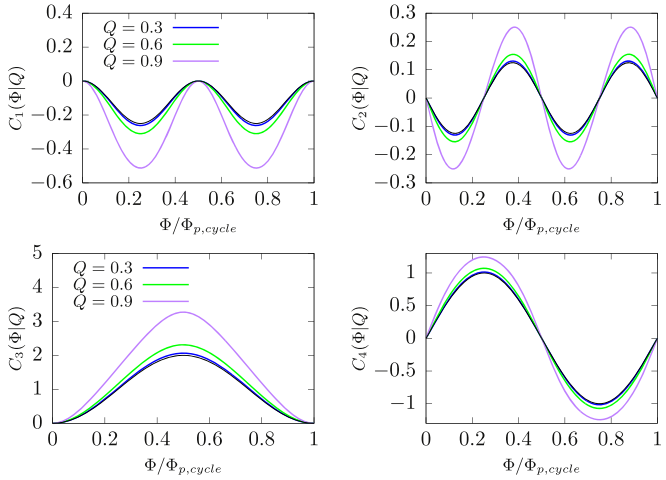

Figure 7. $C_i(\Phi|Q)$ vs. Φ for one precession cycle and $Q = 0$, 0.3, 0.6, and 0.9.

Appendix B
Analytic Theory of Detection Probability

Equation (70) relates the intrinsic intensity I and the peak intensity $I(1)$; in our model a burst is detectable if $I > I_{\rm min}$. The probability that a burst with peak intensity $I(1)$ is detectable at the precession phase Φ is

$$P_{\rm detect}(I(1), \Phi) = \int d^2\hat{\boldsymbol{b}}\, n(\hat{\boldsymbol{b}})\Theta(I - I_{\rm min})$$
$$= \int d^2\hat{\boldsymbol{b}}\, n(\hat{\boldsymbol{b}})\Theta(I(1)\exp[\kappa(\hat{\boldsymbol{b}}\cdot\hat{\boldsymbol{n}}(\Phi) - 1)] - I_{\rm min}),$$

where $n(\hat{\boldsymbol{b}})$ is the distribution of beam directions (normalized to 1) and $\Theta(\cdots)$ is the Heaviside function; use

$$\begin{aligned}&\Theta(I(1)\exp[\kappa(\hat{\boldsymbol{b}}\cdot\hat{\boldsymbol{n}}(\Phi)-1)]-I_{\min})\\&=\Theta((I(1)/I_{\min})\exp[\kappa(\hat{\boldsymbol{b}}\cdot\hat{\boldsymbol{n}}(\Phi)-1)]-1)\\&=\Theta(\ln(I(1)/I_{\min})+\kappa[\hat{\boldsymbol{b}}\cdot\hat{\boldsymbol{n}}(\Phi)-1])\\&=\Theta(\kappa^{-1}\ln(I(1)/I_{\min})-1+\hat{\boldsymbol{b}}\cdot\hat{\boldsymbol{n}}(\Phi))\end{aligned}$$

to rewrite

$$P_{\rm detect}=\int d^2\hat{\boldsymbol{b}}\,n(\hat{\boldsymbol{b}})\Theta(\kappa^{-1}\ln(I(1)/I_{\min})-1+\hat{\boldsymbol{b}}\cdot\hat{\boldsymbol{n}}(\Phi))\,.$$

In a right-handed coordinate system defined by unit vectors $\hat{\boldsymbol{e}}_a$, $\hat{\boldsymbol{e}}_b$, $\hat{\boldsymbol{\mu}}$ let

$$\hat{\boldsymbol{n}}(\Phi)=\hat{\boldsymbol{\mu}}\cos\theta_n+\sin\theta_n(\hat{\boldsymbol{e}}_a\cos\varphi_n+\hat{\boldsymbol{e}}_b\sin\varphi_n)\,,$$

so that

$$\begin{aligned}\hat{\boldsymbol{b}}\cdot\hat{\boldsymbol{n}}(\Phi)&=\cos\theta_b\cos\theta_n+\sin\theta_b\sin\theta_n\cos(\varphi_b-\varphi_n)\\&\equiv\cos\theta_b\cos\theta_n+\sin\theta_b\sin\theta_n\cos\tilde{\varphi}_b\,;\end{aligned}$$

then the Heaviside function requires that

$$1\geqslant\cos\theta_b\cos\theta_n+\sin\theta_b\sin\theta_n\cos\tilde{\varphi}_b>1-\frac{\ln(I(1)/I_{\min})}{\kappa}\,,$$

and therefore $\hat{\boldsymbol{b}}\cdot\hat{\boldsymbol{n}}(\Phi)$ must be close to 1 for very large values of κ. Thus if we define $\theta_b=\theta_n+\delta_b$, where $\delta_b\ll 1$, and assume that $\tilde{\varphi}_b\ll 1$

$$\begin{aligned}&\cos\theta_b\cos\theta_n+\sin\theta_b\sin\theta_n\cos\tilde{\varphi}_b=\cos(\theta_b-\theta_n)\\&+\sin\theta_b\sin\theta_n(\cos\tilde{\varphi}_b-1)\approx 1-\tfrac{1}{2}(\delta_b^2+\sin^2\theta_n\tilde{\varphi}_b^2)\end{aligned}$$

and the Heaviside function requires that

$$\begin{aligned}&1\geqslant 1-\tfrac{1}{2}(\delta_b^2+\sin^2\theta_n\tilde{\varphi}_b^2)>1-\frac{\ln(I(1)/I_{\min})}{\kappa}\\&\Rightarrow 0\leqslant\delta_b^2+\sin^2\theta_n\tilde{\varphi}_b^2<\frac{2\ln(I(1)/I_{\min})}{\kappa}\equiv R^2\,.\end{aligned}$$

We assume that $n(\hat{\boldsymbol{b}})=\tilde{n}(\cos\theta_b)/2\pi$ is only a function of $\cos\theta_b$; with this assumption

$$d^2\hat{\boldsymbol{b}}n(\hat{\boldsymbol{b}})=\frac{d\varphi}{2\pi}\,d\cos\theta_b\,\tilde{n}(\cos\theta_b)\simeq\frac{d\tilde{\varphi}_b}{2\pi}\,d\delta_b\sin\theta_n\,\tilde{n}(\cos\theta_n).$$

With these substitutions we find

$$\begin{aligned}&P_{\rm detect}(I(1),\,\Phi)\simeq\int_{-R}^{+R}d\delta_b\,\sin\theta_n\,\tilde{n}(\cos\theta_n)\\&\times\int_{-\sqrt{R^2-\delta_b^2}/\sin\theta_n}^{+\sqrt{R^2-\delta_b^2}/\sin\theta_n}\frac{d\tilde{\varphi}_b}{2\pi}\\&=\frac{2R^2\tilde{n}(\cos\theta_n)}{\pi}\int_0^1 dx\,\sqrt{1-x^2}=\frac{\tilde{n}(\cos\theta_n)\ln(I(1)/I_{\min})}{\kappa}\end{aligned}\tag{B.1}$$

1. $P_{\rm detect}$ increases with weakly increasing $I(1)$, decreases $\propto 1/\kappa$ as κ increases, and is only nonzero where $n(\cos\theta_n)\neq 0$.
2. If $\tilde{n}(\cos\theta_b)$ is uniform, as would be the case if beam directions are random and isotropic, then there is no Φ dependence so there is no imprint of either the spin frequency or the precession frequency on $P_{\rm detect}$.
3. Precession phase Φ dependence arises from nonuniformity in $\tilde{n}(\cos\theta_b)$; in our models, nonuniformity is a consequence of boundaries in the distribution of beam directions.

Consider the region near $\theta_{\max}$. If $\theta_{\max}-R<\theta_n<\theta_{\max}$ and $\tilde{n}(\cos\theta_b)=0$ at $\theta_b>\theta_{\max}$ then

$$\begin{aligned}P_{\rm detect}(I(1),\,\Phi)&\simeq\frac{\tilde{n}R}{\pi}\int_{-R}^{\theta_{\max}-\theta_n}d\delta_b\,\sqrt{1-\delta_b^2/R^2}\\&=\frac{\tilde{n}R^2}{\pi}\left[\frac{\pi}{4}+\frac{1}{2}(\sin^{-1}\Delta+\Delta\sqrt{1-\Delta^2})\right]\end{aligned}\tag{B.2}$$

where $\Delta=(\theta_{\max}-\theta_n)/R<1$ and $\tilde{n}$ is the uniform value inside the region containing beams; if $\theta_n>\theta_{\max}$ then $-R<\delta_b<\theta_{\max}-\theta_n<0$ and

$$\begin{aligned}P_{\rm detect}(I(1),\,\Phi)&=\frac{\tilde{n}R}{\pi}\int_{-R}^{\theta_{\max}-\theta_n}d\delta_b\sqrt{1-\delta_b^2/R^2}\\&=\frac{\tilde{n}R^2}{\pi}\left[\frac{\pi}{4}-\frac{1}{2}(\sin^{-1}|\Delta|+|\Delta|\sqrt{1-\Delta^2})\right].\end{aligned}\tag{B.3}$$

Equation (B.2) can be used for θ_n inside or outside provided that we use $\sin\Delta=-\sin|\Delta|$ for $\Delta<0$. Near $\theta_{\min}$, similar considerations imply that $-1<\delta_b<\theta_n-\theta_{\min}$; then we get the same results but with $\Delta=(\theta_n-\theta_{\min})/R$. For $\theta_{\min}=0$, $0\leqslant\delta_b\leqslant\theta_n$ $(0\leqslant\Delta\leqslant 1)$. Otherwise, $P_{\rm detect}=0$ for $\theta_n\leqslant\theta_{\min}-R$ and for $\theta_n>\theta_{\max}+R$. These results depend on Φ via Δ and imprint information about both the spin frequency and the precession cycle on our models. We also note that the range of values of θ_n is model-dependent via Λ, e^2, and the rate at which outbursts occur, which may depend on Φ (but does not in our models). If $R(\Phi,\,I(1))dI(1)d\Phi$ is the rate of outbursts with intrinsic intensity in $I(1)+dI(1)$ then

$$dr_{\rm detect}(\Phi)=d\Phi\int dI(1)R(I(1),\,\Phi)P_{\rm detect}(I(1),\,\Phi)\tag{B.4}$$

is the rate of detection of bursts in $d\Phi$.

These results can be generalized to beams distributed about multiple axes by replacing

$$n(\hat{\boldsymbol{b}})\rightarrow\sum_j p_j n_j(\hat{\boldsymbol{b}})$$

where p_j is the probability that a beam comes from the distribution around the axis $\hat{\boldsymbol{\mu}}_j$ and $n_j(\hat{\boldsymbol{b}})$ is normalized to 1. The average beam direction is then the sum of $p_j\langle\hat{\boldsymbol{b}}_j\rangle$.

ORCID iDs

I. Wasserman https://orcid.org/0000-0001-6618-6096
J. M. Cordes https://orcid.org/0000-0002-4049-1882
S. Chatterjee https://orcid.org/0000-0002-2878-1502
G. Batra https://orcid.org/0000-0002-3208-665X

References

Abramowitz, M., & Stegun, I. A. 1972, Handbook of Mathematical Functions (New York: Dover)
Akgün, T., Link, B., & Wasserman, I. 2006, MNRAS, 365, 653
Akgün, T., Miralles, J. A., Pons, J. A., & Cerdá-Durán, P. 2016, MNRAS, 462, 1894

Akgün, T., Reisenegger, A., Mastrano, A., & Marchant, P. 2013, MNRAS, 433, 2445
Akgün, T., & Wasserman, I. 2008, MNRAS, 383, 1551
Alpar, M. A., Pines, D., Anderson, P. W., & Shaham, J. 1984, ApJ, 276, 325
Anderson, P. W., Alpar, M. A., Pines, D., & Shaham, J. 1982, PMagA, 45, 227
Anderson, P. W., & Itoh, N. 1975, Natur, 256, 25
Baym, G., Pethick, C., & Pines, D. 1969, Natur, 224, 673
Braithwaite, J. 2009, MNRAS, 397, 763
Bretz, J., van Eysden, C. A., & Link, B. 2021, MNRAS, 504, 5880
Caplan, M. E., Schneider, A. S., & Horowitz, C. J. 2018, PhRvL, 121, 132701
Cardall, C. Y., Prakash, M., & Lattimer, J. M. 2001, ApJ, 554, 322
Carreau, T., Gulminelli, F., Chamel, N., Fantina, A. F., & Pearson, J. M. 2020, A&A, 635, A84
Chandrasekhar, B. S. 1962, ApPhL, 1, 7
CHIME/FRB Collaboration, Amiri, M., Andersen, B. C., et al. 2020, Natur, 582, 351
Clogston, A. M. 1962, PhRvL, 9, 266
Cordes, J. M. 1993, in ASP Conf. Ser. 36, Planets Around Pulsars, ed. J. A. Phillips, S. E. Thorsett, & S. R. Kulkarni (San Francisco, CA: ASP), 43
Cordes, J. M., Wasserman, I., Chatterjee, S., & Batra, G. 2021, arXiv:2107.12874
Cruces, M., Spitler, L. G., Scholz, P., et al. 2021, MNRAS, 500, 448
Cutler, C. 2002, PhRvD, 66, 084025
Dong, J. M., Lombardo, U., Zhang, H. F., & Zuo, W. 2017, PAN, 80, 77
Frieben, J., & Rezzolla, L. 2012, MNRAS, 427, 3406
Fulde, P., & Ferrell, R. A. 1964, PhRv, 135, 550
Gezerlis, A., Pethick, C. J., & Schwenk, A. 2014, arXiv:1406.6109
Glampedakis, K., Jones, D. I., & Samuelsson, L. 2011, MNRAS, 413, 2021
Glampedakis, K., & Lasky, P. D. 2016, MNRAS, 463, 2542
Goldreich, P. 1970, ApJL, 160, L11
Goldreich, P., & Julian, W. H. 1969, ApJ, 157, 869
Goldreich, P., & Sridhar, S. 1995, ApJ, 438, 763
Gottfried, K. 1966, Quantum Mechanics—Vol. 1: Fundamentals (Reading: W. A. Benjamin)
Gourgouliatos, K. N., & Cumming, A. 2014a, PhRvL, 112, 171101
Gourgouliatos, K. N., & Cumming, A. 2014b, MNRAS, 438, 1618
Gourgouliatos, K. N., & Pons, J. A. 2020, arXiv:2001.03335
Guo, W., Dong, J. M., Shang, X., et al. 2019, NuPhA, 986, 18
Gusakov, M. E., Kantor, E. M., & Ofengeim, D. D. 2017, PhRvD, 96, 103012
Hashimoto, M., Seki, H., & Yamada, M. 1984, PThPh, 71, 320
Haskell, B., & Sedrakian, A. 2018, in The Physics and Astrophysics of Neutron Stars, ed. L. Rezzolla et al. (Cham: Springer), 401
Henriksson, K. T., & Wasserman, I. 2013, MNRAS, 431, 2986
Iroshnikov, P. S. 1963, AZh, 40, 742
Jones, P. B. 1975, Ap&SS, 33, 215
Kinnunen, J. J., Baarsma, J. E., Martikainen, J.-P., & Törmä, P. 2018, RPPh, 81, 046401
Kiuchi, K., & Yoshida, S. 2008, PhRvD, 78, 044045
Kraichnan, R. H. 1965, PhFl, 8, 1385
Lander, S. K., & Gourgouliatos, K. N. 2019, MNRAS, 486, 4130
Lander, S. K., & Jones, D. I. 2012, MNRAS, 424, 482
Lander, S. K., & Jones, D. I. 2017, MNRAS, 467, 4343
Larkin, A. I., & Ovchinnikov, Y. N. 1974, JETP, 38, 854
Lasky, P. D., & Melatos, A. 2013, PhRvD, 88, 103005
Lee, T.-G., Yoshiike, R., & Tatsumi, T. 2018, in JPS Conf. Proc. 20, Workshop on Quarks and Compact Stars 2017 (QCS2017) (Tokyo: Physical Society of Japan), 011006
Levin, Y., Beloborodov, A. M., & Bransgrove, A. 2020, ApJL, 895, L30
Li, D., Wang, P., Zhu, W. W., et al. 2021, Natur, 598, 267
Li, J., Spitkovsky, A., & Tchekhovskoy, A. 2012, ApJ, 746, 60
Li, X., Levin, Y., & Beloborodov, A. M. 2016, ApJ, 833, 189
Link, B. 2003, PhRvL, 91, 101101
Link, B., & Cutler, C. 2002, MNRAS, 336, 211
Link, B., & Epstein, R. I. 2001, ApJ, 556, 392
Link, B., Epstein, R. I., & Baym, G. 1993, ApJ, 403, 285
Link, B., & van Eysden, C. A. 2016, ApJL, 823, L1
Lorenz, C. P., Ravenhall, D. G., & Pethick, C. J. 1993, PhRvL, 70, 379
Mahlmann, J. F., Akgün, T., Pons, J. A., Aloy, M. A., & Cerdá-Durán, P. 2019, MNRAS, 490, 4858
Melatos, A. 1999, ApJL, 519, L77
Melatos, A. 2000, MNRAS, 313, 217
Mestel, L., Nittmann, J., Wood, W. P., & Wright, G. A. E. 1981, MNRAS, 195, 979
Mestel, L., & Takhar, H. S. 1972, MNRAS, 156, 419
Mitchell, J. P., Braithwaite, J., Reisenegger, A., et al. 2015, MNRAS, 447, 1213
Mutafchieva, Y. D., Chamel, N., Stoyanov, Z. K., Pearson, J. M., & Mihailov, L. M. 2019, PhRvC, 99, 055805
Nittmann, J., & Wood, W. P. 1981, MNRAS, 196, 491
Passamonti, A., Akgün, T., Pons, J. A., & Miralles, J. A. 2017, MNRAS, 465, 3416
Pethick, C. J., & Potekhin, A. Y. 1998, PhLB, 427, 7
Potekhin, A. Y., & Chabrier, G. 2018, A&A, 609, A74
Press, W. H., Teukolsky, S. A., Vetterling, W. T., & Flannery, B. P. 2002, Numerical Recipes in C++ : The Art of Scientific Computing (Cambridge: Cambridge Univ. Press)
Rau, P. B., & Wasserman, I. 2021, MNRAS, 506, 4632
Ravenhall, D. G., Pethick, C. J., & Wilson, J. R. 1983, PhRvL, 50, 2066
Reisenegger, A. 2009, A&A, 499, 557
Reisenegger, A., & Goldreich, P. 1992, ApJ, 395, 240
Schneider, A. S., Caplan, M. E., Berry, D. K., & Horowitz, C. J. 2018, PhRvC, 98, 055801
Shaham, J. 1977, ApJ, 214, 251
Spitzer, L., Jr. 1958, in IAU Symp. 6, Electromagnetic Phenomena in Cosmical Physics, ed. B. Lehnert (Cambridge: Cambridge Univ. Press), 169
Suh, I.-S., & Mathews, G. J. 2010, ApJ, 717, 843
The CHIME/FRB Collaboration, Andersen, B. C., Bandura, K., et al. 2021, arXiv:2107.08463
Thompson, C., & Duncan, R. C. 1993, ApJ, 408, 194
Wasserman, I. 2003, MNRAS, 341, 1020
Zanazzi, J. J., & Lai, D. 2020, ApJL, 892, L15
Zhang, Y. G., Gajjar, V., Foster, G., et al. 2018, ApJ, 866, 149
Zuo, W., Cui, C. X., Lombardo, U., & Schulze, H. 2008, PhRvC, 78, 015805